J. Fluid Mech. (2023), *vol.* 974, A36, doi:10.1017/jfm.2023.756

The role of rolling resistance in the rheology of wizarding quidditch ball suspensions

Enzo d'Ambrosio[1], **Donald L. Koch**[1] **and Sarah Hormozi**[1],†

[1]Robert Frederick Smith School of Chemical and Biomolecular Engineering, Cornell University, Ithaca, NY 14853, USA

(Received 23 January 2023; revised 22 June 2023; accepted 5 September 2023)

To elucidate the effect of particle shape on the rheology of a dense, viscous suspension of frictional, non-Brownian particles, experimental measurements are presented for suspensions of polystyrene particles with different shapes in the same solvent. The first suspension is made of spheres whereas the particles which compose the second suspension are globular but with flattened faces. We present results from steady shear and shear-reversal rheological experiments for the two suspensions over a wide range of stresses in the viscous regime. Notably, we show that the rheology of the two suspensions is characterised by a shear-thinning behaviour, which is stronger in the case of the suspension of globular particles. Since the shear-reversal experiments indicate an absence of adhesive particle interactions, we attribute the shear thinning to a sliding friction coefficient which varies with stress as has been observed previously for systems similar to the first suspension. We observe that the viscosity of the two suspensions is similar at high shear stress where small sliding friction facilitates particle relative motion due to sliding. At lower shear stress, however, the sliding friction is expected to increase and the particle relative motion would be associated with rolling. The globular particles attain a higher viscosity at low shear stress than the spherical particles. We attribute this difference to a shape-induced resistance to particle rolling that is enhanced by the flattened faces. Image analysis is employed to identify features of the particle geometry that contribute to the resistance to rolling. It is shown that the apparent rolling friction coefficients inferred from the rheology are intermediate between the apparent dynamic and static rolling friction coefficients predicted on the basis of the image analysis. All three rolling resistance estimates are larger for the globular particles with flat faces than for the spherical particles and we argue that this difference yields the stronger shear thinning of the globular particle suspension.

Key words: suspensions, rheology

† Email address for correspondence: hormozi@cornell.edu

1. Introduction

Non-Brownian suspensions made of relatively rigid particles are ubiquitous in industry (fresh concrete, civil engineering, rocket fuel, etc.) and in natural flows (mud, lava flows, submarine avalanches, etc.). This widespread occurrence has encouraged active research in the past years that has revealed great complexity in the behaviour of these systems, which are usually composed of particles with irregular shape. Notably, it has been shown that even the simplest suspension, a non-Brownian suspension made of relatively rigid, single-sized rough spheres (of radius a) with negligible colloidal forces (no adhesion), suspended in a density-matched (no effect of gravity) Newtonian fluid (of viscosity η_0) and sheared in a viscous creeping flow (no inertial effect), can exhibit a rich variety of rheological behaviours. The best known feature is the divergence of shear viscosity, η, when the solid volume fraction, ϕ, tends to a maximum value known as the jamming volume fraction, ϕ_m. However, the range of complex rheological behaviours can also include the occurrence of a yield stress (Dagois-Bohy *et al.* 2015; Ovarlez *et al.* 2015), shear-thinning (Vázquez-Quesada, Tanner & Ellero 2016; Lobry *et al.* 2019) or shear-thickening behaviours (Barnes 1989; Mari *et al.* 2014; Guy, Hermes & Poon 2015; Comtet *et al.* 2017; Madraki *et al.* 2017; Madraki, Ovarlez & Hormozi 2018; Madraki *et al.* 2020), normal stress differences, irreversibility under oscillating shear (Pine *et al.* 2005; Blanc, Peters & Lemaire 2011*a*), shear-induced microstructure (Gadala-Maria & Acrivos 1980; Blanc *et al.* 2011*a*, 2013) and particle migration (Phillips *et al.* 1992; Snook, Butler & Guazzelli 2016; Sarabian *et al.* 2019; Rashedi, Ovarlez & Hormozi 2020).

Owing to the complexity already present in the 'simplest system', suspensions made of spheres have been studied extensively for decades. In contrast, the role played by the particle shape has only started to be investigated recently and still suffers from a dearth of experimental data. Yet, many suspensions found in industry and in nature are composed of globular particles, which have an irregular compact form with a global aspect ratio close to 1 (see figure 1). These particles are predominantly convex due to erosion. The present paper describes an experimental work that aims at reducing this deficit by studying the rheology of a viscous non-Brownian frictional suspension made of globular particles ($2a \sim 40$ µm) and comparing it with a suspension of spheres made of the same solid material and suspended in the same solvent. For this purpose, some polystyrene (PS) beads have been crushed, while others have not, in order to create two similar suspensions (described in § 2): one made of beads (see the first sketch from the left in figure 1) and the other made of particles with irregular globular shapes (see the third sketch from the left in figure 1). Since the recent works of Le *et al.* (2023) have shown that the rheology of a suspension depends strongly both on the type of particles and the solvent, it is important to note that both types of PS particles studied in the present paper are separately dispersed in the same suspending liquid (silicone oil). Therefore, the only difference between the two types of suspension studied in the present paper is the solid particle shape and we investigate the role of shape disentangled from other factors.

In the last decade, the central role played by direct solid contact in the flow properties of non-Brownian frictional suspensions has been revealed by Boyer, Guazzelli & Pouliquen (2011), who succeeded in applying a granular paradigm to describe the rheological behaviour of non-Brownian and non-colloidal spheres suspended in a Newtonian fluid in the dense regime, showing the key role played by solid contact interactions between particles, existing thanks to their asperities. Later, using a discrete-element method (DEM)-like approach Gallier *et al.* (2014) have extensively studied the influence of asperity height, h_r, and sliding friction coefficient, μ_s, between spheres on the rheology of suspensions. They have notably shown that μ_s is a key parameter that governs the flow (*a*) (*b*) (*c*)

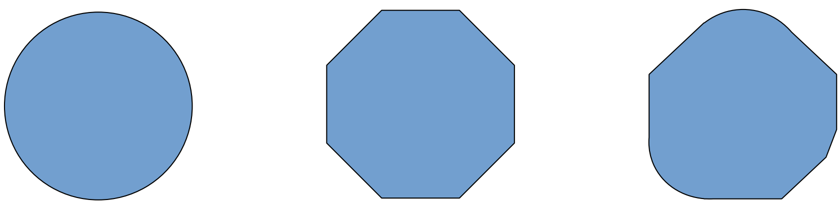

Figure 1. Schematic of different types of 2D-projected particle shapes (from the left to the right): a simple sphere (disc), a regular polyhedron (polygon) and a globular/crushed particle that possesses flat faces and spherical arcs.

properties of frictional suspensions of spheres in the concentrated regime ($\phi > 0.40$). Several numerical studies (Gallier *et al.* 2014; Mari *et al.* 2014; Wyart & Cates 2014; Peters *et al.* 2016; Singh *et al.* 2018) have then shown that μ_s changes the value of the jamming volume fraction, ϕ_m. For instance, Seto *et al.* (2013) and Mari *et al.* (2014) have shown that the proliferation of frictional contacts is known to be the cause of the discontinuous shear-thickening (DST) observed in highly concentrated suspensions of spheres when the shear stress is high enough to overcome repulsive interactions between particles and push them into contact. As a consequence, the authors have measured, in the case of spherical particles, a decay of ϕ_m from 0.66 to 0.58 when μ_s increases from 0 (frictionless case) to 1 (frictional), in qualitative agreement with the experimental values from the literature for frictional suspensions of spheres: $\phi_m \in [0.54; 0.62]$ (Zarraga, Hill & Leighton 2000; Ovarlez, Bertrand & Rodts 2006; Boyer *et al.* 2011; Blanc, Peters & Lemaire 2011*b*; Blanc *et al.* 2018). Later, Peters *et al.* (2016) numerically found that ϕ_m decreases from 0.7 to 0.56 for the same variation of μ_s ($0 \leqslant \mu_s \leqslant 1$), in quite good agreement with these previous works. Moreover, recent experimental studies have directly measured the values of μ_s by atomic force microscopy (AFM) measurements between pairs of PS beads suspended in silicone oil (Arshad *et al.* 2021; Le *et al.* 2023). They found that $0.1 \lesssim \mu_s \lesssim 4$, which confirms the considered range of the values of μ_s in the numerical studies.

Shear-thinning is common in viscous non-Brownian suspensions (Gadala-Maria & Acrivos 1980; Zarraga *et al.* 2000; Dbouk, Lobry & Lemaire 2013; Vázquez-Quesada *et al.* 2016, 2017; Blanc *et al.* 2018; Gilbert, Valette & Lemaire 2022) and can have different physical origin, depending both on the physical properties of the suspension and the range of applied shear stress, Σ_{12} (the indices 1, 2 and 3 referring to the flow, gradient and vorticity directions, respectively). By studying a non-Brownian suspension made of polyvinyl chloride (PVC) particles suspended in a 1,2-cyclohexane dicarboxylic acid diisononyl ester (DINCH, Newtonian oil), Chatté *et al.* (2018) have notably proposed the possible existence of two successive regimes of shear-thinning behaviour separated by a shear-thickening regime related to the frictionless–frictional transition. The first shear-thinning regime occurs at small stress, when the suspension remains frictionless since repulsion prevents direct solid particle contacts. This system can be actually seen as a suspension of 'soft' particles, composed of a 'hard core' (of diameter $d = 2a$) to which a frictionless jacket of thickness, ξ, is added. The gap 2ξ between neighbouring particles is determined by balancing the normal force F_N induced by the applied stress with the colloidal repulsive force, f_N. When Σ_{12} (and therefore the normal force F_N between particles) increases, ξ decreases, and so the apparent size of the particles decreases, $a_{app} = a + \xi(f_N)$, inducing a decay of the apparent volume fraction of the suspension and, *in fine*, a decay of η (Krieger 1972; Maranzano & Wagner 2001*a*). When the particle pressure increases more and overcomes the repulsive forces ($F_N \geqslant f_N^C$), the particles enter increasingly frequently into direct solid contact thanks to their asperities and the suspension passes from a frictionless state to a frictional one.

Interestingly, Mari *et al.* (2014) have shown that the onset of this frictionless–frictional transition ('*fft*') occurs for a critical shear stress (and not a shear rate, $\dot{\gamma}$): $\sigma_{in}^{fft} \approx 0.3 \times f_N^C/(6\pi a^2)$ for spheres, whose value is independent of ϕ as already observed in many experiments (Bender & Wagner 1996; Frith *et al.* 1996; Maranzano & Wagner 2001*a*,*b*; Lootens *et al.* 2005; Fall *et al.* 2010; Larsen *et al.* 2010; Brown & Jaeger 2012, 2014). The authors have also shown that the stress range over which thickening occurs remains constant. This has motivated us to control the applied shear stress in the present study, instead of the shear rate. Once the load F_N is large enough ($F_N \gg f_N^C$), the direct solid contacts between particles saturate since all the particles in the suspension have contacts with their neighbours: the system is in the frictional state. Mari *et al.* (2014) have measured the occurrence of this second regime at $\sigma_{out}^{fft} \sim f_N^C/a^2$.

In the frictional state, if Σ_{12} increases further, then a potential second shear-thinning regime can be observed. We want to emphasise that it is precisely this second shear-thinning regime (when the suspension is frictional) that will be explored in the present paper. The physical origin of this complex behaviour remains an open question. For instance, Acrivos, Fan & Mauri (1994) suggested that the apparent shear-thinning behaviour observed in Couette flow can be due to a difference of density, $\Delta\rho$, between the solid particles and the suspending fluid. Indeed, solid particles heavier than the suspending fluid settle because of gravity and form a more concentrated layer. Then, shear-induced viscous resuspension (Gadala-Maria 1979; Acrivos, Mauri & Fan 1993; Zarraga *et al.* 2000; Saint-Michel *et al.* 2019; d'Ambrosio, Blanc & Lemaire 2021) tends to homogenise the suspension when Σ_{12} increases, which induces an apparent decay of the viscosity. However, while this mechanism may arise in some experiments with Couette rheometers, it cannot explain the shear-thinning behaviour observed in other types of flow. For instance, in the case of a parallel plates geometry, the shear-induced viscous resuspension would tend to increase the viscosity. In addition, we show that Σ_{12} in the present study is large enough so that gravity would not cause significant deviation from uniform volume fraction, so the effect of any shear rate dependence related to gravity is absent.

Lastly, numerical simulations (Lobry *et al.* 2019) and experimental studies (Chatté *et al.* 2018; Arshad *et al.* 2021; Le *et al.* 2023) have shown that the shear-thinning behaviour observed for concentrated viscous non-Brownian frictional suspensions (i.e. beyond the DST) could be related to a sliding friction between solid particles that varies with the normal force F_N. Following the model from Brizmer, Kligerman & Etsion (2007), Lobry *et al.* (2019) have considered that the contact between particles is elastic and occurs only through a few hemisphere-like asperities. In these conditions and according to the Hertz theory, the elastic contact area $A_{contact}$ is proportional to $F_N^{2/3}$ which gives

$$\mu_s = \frac{F_T}{F_N} \propto \frac{A_{contact}}{F_N} \propto F_N^{-1/3}, \tag{1.1}$$

where F_T denotes the tangential force. This model is in good agreement with experimental works (Chatté *et al.* 2018; Arshad *et al.* 2021; Le *et al.* 2023) which have directly determined the decay of μ_s with the normal force F_N by conducting AFM measurements between pairs of particles. Arshad *et al.* (2021) and Le *et al.* (2023) have conducted AFM measurements to measure the pairwise friction between pairs of PS beads ($d \approx 40$ μm) immersed in an aqueous liquid and silicone oil, respectively. Note that the system of suspension studied by Le *et al.* (2023) is the same as that studied in the present paper. The different studies (Lobry *et al.* 2019; Arshad *et al.* 2021; Le *et al.* 2023) performed on suspensions of spherical particles have all converged to the following equation based on the works from Brizmer *et al.* (2007):

$$\mu_s = \mu_s^\infty \times \coth\left[\mu_s^\infty \left(\frac{F_N}{L_c}\right)^m\right], \tag{1.2}$$

where L_c corresponds to the critical normal force which scales the saturation of μ_s. In other words, the sliding friction coefficient becomes constant and equal to μ_s^∞ when $F_N \gg L_c$, because of an elastic to plastic transition of asperities deformation (Lobry *et al.* 2019). In the case of a contact between a perfectly smooth half sphere and a flat surface, Brizmer *et al.* (2007) determined: $\mu_s^\infty = 0.27$ and $m = 0.35$, whereas Lobry *et al.* (2019) estimated $L_c = 20$ nN based on the material properties (PS particles). More recently, Arshad *et al.* (2021) directly measured $\mu_s^\infty = 0.18$ by AFM measurements and determined $L_c = 33.2$ nN and $m = 0.54$ by fitting their experimental results obtained for PS particles in an aqueous liquid by (1.2). On the other hand, Le *et al.* (2023) measured for PS beads in silicone oil: $\mu_s^\infty = 0.15$ ($m = 0.4$). Note that, since the particles of the suspensions studied in the present paper are of the same chemical composition found in these studies from the literature (and even the same solvent for Le *et al.* 2023), we reuse (1.2) coupled with the latter constants to characterise the shear-thinning behaviour of the studied suspensions.

Lobry *et al.* (2019) have numerically determined the relationship between the normal force applied on spherical particles and the shear stress: $F_N = 6\pi a^2 \Sigma_{12}/1.69$. Equivalently, a critical shear stress, Σ_c, can be defined as $L_c = 6\pi a^2 \Sigma_c/1.69$, which allows one to obtain the following updated equation for the variable sliding friction coefficient:

$$\mu_s = \mu_s^\infty \times \coth\left[\mu_s^\infty \left(\frac{\Sigma_{12}}{\Sigma_c}\right)^m\right]. \tag{1.3}$$

It is known in granular media that the two possible motions for a particle are sliding (characterised by μ_s) and rolling. The one offering the least resistance will be favoured but both can obviously occur at the same time in a sheared suspension (Estrada, Taboada & Radjai 2008). One can easily understand that the particle shape might have a significant effect on one or even both of these motions, depending on the contact between particles. A decade ago, the numerical simulations of Estrada *et al.* (2011) in granular media have shown that the way a non-spherical shape provides resistance to rolling can be essentially modelled by approximating the non-spherical particle (like a globular one) by a sphere ‘equipped’ with an apparent rolling resistance torque, Γ_{F_N} (see figure 2). This shape-induced rolling resistance would be therefore characterised by a rolling friction coefficient, μ_r, defined from a Coulomb-type law:

$$F_N^t \leqslant \mu_r F_N. \tag{1.4}$$

This is the sense in which we will consider rolling friction in the present paper. It is important to note that the main assumption that we make in the present paper is then to approximate the three-dimensional (3D) globular particles (irregular polyhedra) by their two-dimensional (2D)-projected shapes (irregular polygons).

Recent numerical simulations from Singh *et al.* (2020) have notably predicted a decay of ϕ_m when μ_r increases, but a dearth of experimental data remains preventing verification of this important insight. Thus, in the present paper, after describing the experimental process in § 2, we first aim (in § 3) at measuring the jamming volume fraction, ϕ_m,

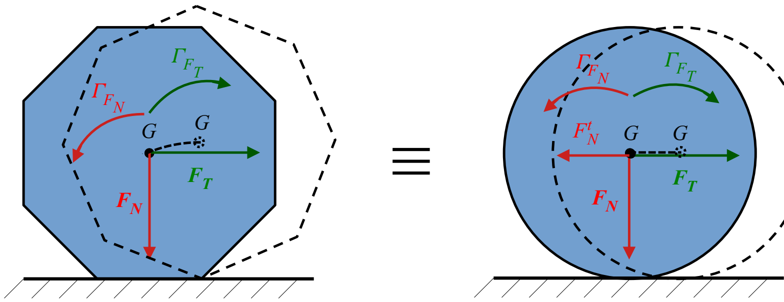

Figure 2. Schema of rolling on a plane from the left to the right for a regular octagon (on the left) and a disc (on the right), thanks to a tangential force, $\boldsymbol{F_T}$, applied at the centre of mass G of the particles. The two particles have the same perimeter. The two systems can be considered equivalent if the disc is 'equipped' with a rolling resistance torque, Γ_{F_N}, directly related to a 'rolling resistance force', $\boldsymbol{F_N^t}$ defined from the normal force, $\boldsymbol{F_N}$, applied on G as $F_N^t \leqslant \mu_r F_N$. Here, μ_r is the rolling friction coefficient (Estrada *et al.* 2008, 2011).

of the two studied suspensions, in order to characterise the rheological behaviour of non-Brownian viscous suspensions made of frictional particles with irregular shapes and compare it with the rheology of a basic suspension made of spheres of the same material. In the second part, we then determine by an image analysis process (see § 4) the rolling friction coefficient, μ_r, of the studied globular particles in order to compare the numerical predictions of ϕ_m from the literature with our own experimental data.

2. Experimental methods

2.1. *Suspensions*

In this paper, the rheological behaviour of two different non-Brownian viscous suspensions are investigated. The two suspensions are very similar: they are both made of the same PS particles (TS40, Microbeads) with a density measured as $\rho_p = 1.06$ g cm^{-3} and sieved between 36 and 45 µm in order to reduce the initially large size distribution, dispersed separately in the same solvent, a Newtonian silicone oil (Sigma-Aldrich) of density $\rho_f = 0.97$ g cm^{-3} and viscosity $\eta_0 = 0.98$Pa s measured at $T = 23\,^{\circ}$C. To prepare a given suspension, a known mass of solid particles is carefully mixed with a known mass of liquid. The air bubbles are then removed by putting the sample in an ultrasound bath. The suspension is finally gently stirred in order to resuspend the particles that would have settled during the degassing procedure.

The only difference between the two suspensions remains in the shape of the PS particles. For the first suspension, labelled S_{PS40}, the solid particles are spheres and to make the second suspension labelled C_{PS40}, the PS particles have been crushed by a process described in Appendix A. Figure 3 shows examples of these particles captured with a basic microscope: some spherical particles are presented in figure 3(*a*) whereas a sample of crushed particles is shown in figure 3(*b*). One can already note that the population of crushed particles is slightly heteroclyte, being composed of different shapes classified from simple spheres to more facetted particles and particles having both spherical and flat surfaces (see the rightmost schematic in figure 1). It is this appearance, combining spherical arcs and flat surfaces similarly to a quidditch ball (the so-called *quaffle*), which motivated us to choose the title for the present paper. Figure 4 displays an enlarged image of a sample of crushed PS particles, which allows one to better appreciate this heteromorphism.

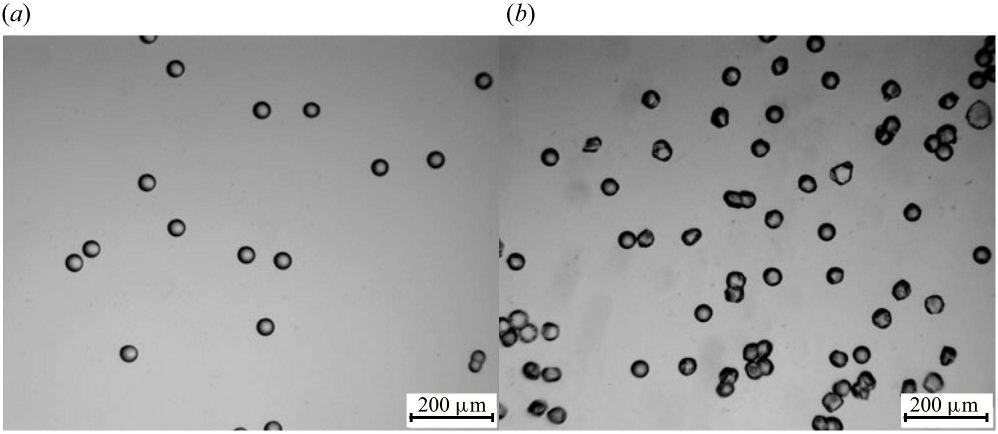

Figure 3. (*a*) Spherical PS particles. (*b*) Crushed PS particles. Scale ≈ 1.75 px $(\mu m)^{-1}$. Particle diameter: $d = 2a \sim 40\ \mu m$.

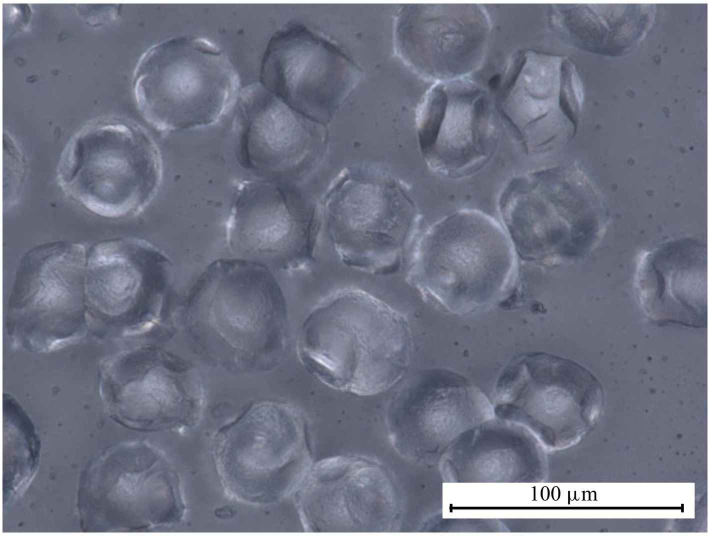

Figure 4. Globular/crushed PS particles composing C_{PS40}.

A quantitative study by image analysis has been conducted over a few hundred images captured with a microscope such as those presented in figure 3 in order to characterise the size distribution of the two types of particles, displayed in figure 5. One can observe that the spherical and crushed PS particles have roughly the same size, and both populations can be considered monodisperse with mean and standard deviation of the diameter of $\langle d\rangle^{S_{PS40}} \approx (42 \pm 1)\ \mu m$ and $\langle d\rangle^{C_{PS40}} \approx (43 \pm 4)\ \mu m$. If the crushed particles appear slightly larger than the spherical particles, it is likely due to the fact that the diameter d is calculated from the projected area of the particle.

2.2. *Rheometry experiments*

Rheometric experiments are carried out in a controlled-stress rheometer HR30 (TA instruments) with a smooth rotating parallel plate of radius $R = 20$ mm. The temperature

https://doi.org/10.1017/jfm.2023.756 Published online by Cambridge University Press

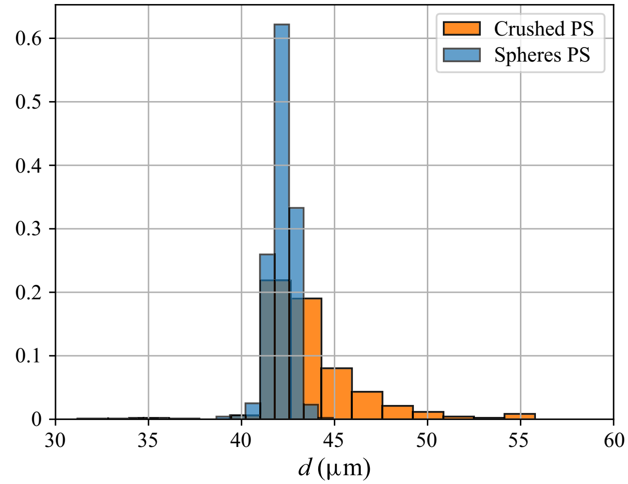

Figure 5. Size distribution of spheres (blue) and crushed particles (orange). For a crushed particle, the projected area, denoted A_p, is measured by microscopic image analysis. The diameter d corresponds to the diameter of a disc having the same area as the projected crushed particle: $d = 2 \times \sqrt{A_p/\pi}$.

is controlled by the static lower plate and is set at $T = 23\,^{\circ}\mathrm{C}$ for all the experiments. The gap is imposed at $1\ \mathrm{mm} \lesssim h \lesssim 2\ \mathrm{mm}$, which allows one to have enough particles ($20 \lesssim h/d \lesssim 50$) to minimise phenomena of layering and sliding. The preference of working in a parallel rotating disc is led by the near absence of shear-induced particle migration in such a geometry (Chow *et al.* 1994; Merhi *et al.* 2005), which helps in keeping a homogeneous suspension across the gap. However, the drawback of this geometry is that the shear rate is not constant. Indeed, $\dot{\gamma}$ increases from 0 at the centre to $\dot{\gamma}_R = \varOmega R/h$ at $r = R$, with $\varOmega$ the angular velocity of the upper rotating plate. In the case of a non-Newtonian behaviour, this variation can be problematic since the viscosity of the suspension, η, depends on the shear rate, $\dot{\gamma}$. In order to take into account this experimental bias and deduce the correct values of η, we use the well-known Mooney–Rabinowitsch correction:

$$\eta = \eta_{app}\left[1 + \frac{1}{4}\frac{\mathrm{d}\ln(\eta_{app})}{\mathrm{d}\ln(\dot{\gamma}_R)}\right], \tag{2.1}$$

where η_{app} is the apparent viscosity deduced by the rheometer from the measurements of shear rate at the rim of parallel plates, $\dot{\gamma}_R$, and applied torque, $\varGamma$,

$$\eta_{app} = \frac{2}{\pi R^3}\frac{\varGamma}{\dot{\gamma}_R}. \tag{2.2}$$

We studied the rheological behaviour of each suspension over a wide range of shear stress, $\varSigma_{12} \in [5, 100]$ Pa, and solid volume fraction, $\phi \in [0.43, 0.51]$. Note that we work with a volume-imposed geometry and being sure of the volume fraction ϕ present in the gap is critical for our experiments. It is very difficult to prepare a proper sample with a known volume fraction when ϕ is close to the jamming volume fraction, ϕ_m. This could be due to the presence of air bubbles hard to remove, instantaneous shear-induced migration when the sample is poured into the gap or even a yield stress which may prevent the suspension from flowing into the gap by gravity. For these reasons, the maximum value for ϕ in the experiments was kept at 0.51. For each $\varSigma_{12}$ and each ϕ (in total, 50 combinations of $(\phi, \varSigma_{12})$), a shear reversal experiment was performed. We encourage the readers to consult Blanc *et al.* (2018) for details on the protocol. Briefly, the suspension is simply sheared at a given constant Σ_{12}. Once the steady state has been reached (η is constant), the flow direction is reversed while the value of Σ_{12} is kept constant. Then, the suspension is sheared in this new direction until the steady value of η is retrieved. For each ϕ on both types of suspension, a series of shear-reversal experiments was performed on two independent samples. The results in the following correspond to the average of these two independent measurements.

Within these conditions, the values of the Péclet and Reynolds numbers characterise the suspension as non-Brownian and its flow as viscous (inertial effects are negligible), respectively:

$$Pe = \frac{6\pi \Sigma_{12} a^3}{k_B T} > 10^8 \quad \text{and} \quad Re = \frac{\rho_f \Sigma_{12} h^2}{\eta_0^2} < 0.1, \tag{2.3a,b}$$

with k_B the Boltzmann constant. At the same time, note that the Stokes number is kept small throughout all the experiments: $St = (\frac{1}{18})\rho_p d^2 \Sigma_{12}/\eta^2 < 10^{-5}$. It is thus expected that only viscous and contact forces govern the suspension behaviour.

The maximum shear stress ($\Sigma_{12} = 100$ Pa) is set by the occurrence of edge fracture which is expected for a first normal stress of the order of the capillary pressure (Keentok & Xue 1999): $N_1 \approx 2\gamma_{air\text{-}oil}/h$, with the surface tension of silicone oil, $\gamma_{air\text{-}oil} \approx 30$ mN m^{-1}. Since the literature shows $N_1 \lesssim 0.5\Sigma_{12}$, we obtain the following criterion to avoid edge fracture: $\Sigma_{12} \lesssim 120$ Pa, a value close to experimental observations. On the other hand, the minimum stress ($\Sigma_{12} = 5$ Pa) is chosen in such a way that the Shield number, denoted Sh, is large enough ($Sh \gg 1$) to ensure that the particles do not settle due to the slight difference of density, $\Delta\rho$, between the solid and liquid phases, and that a vertical homogeneous suspension is maintained throughout the entire experimental procedure:

$$Sh = \frac{\Sigma_{12}}{\Delta\rho g d} \gtrsim 10^2 \quad \text{with } \Delta\rho = \rho_p - \rho_f = (0.09 \pm 0.02)\ \text{g cm}^{-3}. \tag{2.4}$$

We want to underline that AFM measurements found in the literature (Le *et al.* 2023) do not observe any repulsive forces before contact for PS particles (also from Microbeads) in a silicone oil (from Merck, $\rho_f = 0.95$ g cm^{-3}, $\eta_0 \approx 20$ mPa s at 25 °C), meaning that we are already in the frictional regime for the range of Σ_{12} studied in the present paper, and that particles are in contact even when $\dot{\gamma} \to 0$. This will be confirmed later by the measured values of ϕ_m and the comparison with the literature (Gallier *et al.* 2014; Mari *et al.* 2014; Peters *et al.* 2016).

To conclude this section on the rheometry, we want to emphasise that the plate surfaces are smooth and we made sure that there was no wall slip phenomenon by measuring the viscosity of the suspensions at the largest volume fraction for different gap size. A viscosity found to be independent of the height of the upper plate indicates that there is no detectable wall slip (Yoshimura & Prud'homme 1988).

3. Results and discussion on macroscopic rheological measurements

3.1. *Rheological measurements*

In this section, we aim to characterise the rheological behaviour of the suspension made of crushed PS particles (C_{PS40}) and compare it with our measurements of the rheology of the suspension made of spherical PS particles (S_{PS40}), which is more common in the literature.

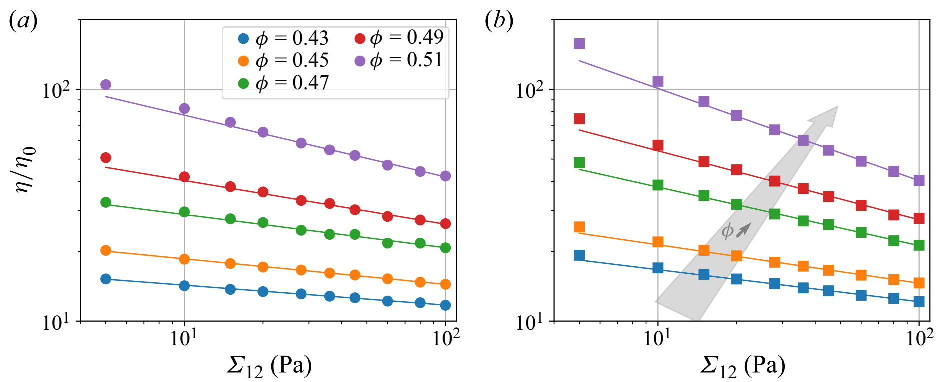

Figure 6. Variation of the measured relative steady viscosity, $\eta_r = \eta/\eta_0$, with applied shear stress Σ_{12} for (*a*) the suspension S_{PS40} made of spherical PS beads and (*b*) C_{PS40} made of crushed PS particles. Each colour labels a solid volume fraction ϕ: 0.43 (blue), 0.45 (orange), 0.47 (green), 0.49 (red) and 0.51 (purple). For each given ϕ, the experimental measurements (coloured dot) are fitted by a power law (coloured straight line): $\Sigma_{12} = K\dot{\gamma}^n$ with $\dot{\gamma} = \Sigma_{12}/\eta$. The resulting parameters of these fits are shown in figure 8.

3.1.1. *Steady viscosity*

Figure 6 displays the variation of the measured relative steady viscosity, $\eta_r = \eta/\eta_0$, with applied shear stress, Σ_{12}, for (*a*) the suspension S_{PS40} made of spherical PS particles and (*b*) C_{PS40} made of crushed PS particles. Each coloured point corresponds to an experimental measurement of η_r (relative viscosity corrected by (2.1)) at a given ϕ and a given Σ_{12}. The relative uncertainty for each measurement, not represented on the graphs in figure 6 in order to keep them clear, is always smaller than 5 %.

The values of viscosity measured on S_{PS40} within the explored range of Σ_{12} are in quite good agreement with other previous works present in the literature (Blanc *et al.* 2018; Lobry *et al.* 2019; Le *et al.* 2023) and conducted on an identical system (i.e. PS spheres of size close to 40 µm dispersed in silicone oil). It appears in figure 6 that C_{PS40} exhibits a rheological behaviour which is broadly similar to that which characterises S_{PS40}. In particular, we observe for both suspensions that:

(i) as expected, η_r increases with ϕ for a given Σ_{12};
(ii) η_r decreases with Σ_{12} for a given ϕ, qualifying the non-Newtonian behaviour in the range of applied shear stress ($\Sigma_{12} \in [5\text{–}100]$ Pa) for both suspensions as shear-thinning;
(iii) as expected, the decay of η_r with Σ_{12} is steeper (meaning the shear-thinning behaviour is more pronounced) at large ϕ.

On the other hand, the primary distinction between the suspensions is that the shear-thinning behaviour is stronger for C_{PS40} compared with S_{PS40} for a given ϕ. Figure 7 displays the normalised difference of relative viscosity between the two suspensions, $(\eta_r^{C_{PS40}} - \eta_r^{S_{PS40}})/\eta_r^{S_{PS40}}$, as function of the applied shear stress Σ_{12}. One can then easily observe that the suspension made of crushed particles is more viscous than the suspension made of spherical particles at low shear stress, whereas the viscosities of the two suspension are nearly the same at high shear stress.

According to the literature (Coussot & Piau 1994; Schatzmann, Fischer & Bezzola 2003; Sosio & Crosta 2009; Mueller, Llewellin & Mader 2010; Vance, Sant & Neithalath 2015), we can quantify the non-Newtonian behaviour of such suspensions by fitting the

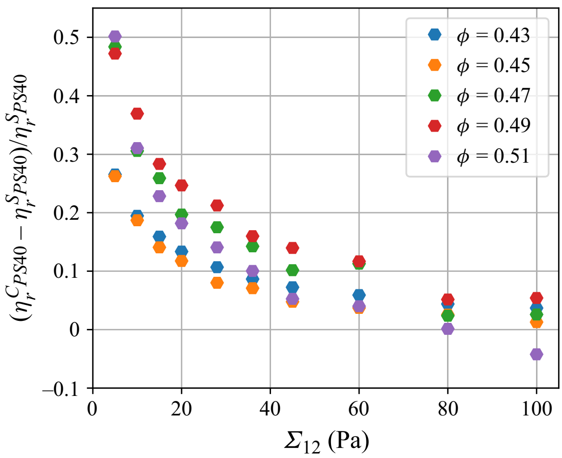

Figure 7. Variation of the measured relative steady viscosity difference between C_{PS40} and S_{PS40}, $\eta_r^{C_{PS40}} - \eta_r^{S_{PS40}}$, normalised by the measured relative steady viscosity for the suspension made of spherical PS particles, $\eta_r^{S_{PS40}}$, as function of the applied shear stress Σ_{12}. Each colour labels the solid volume fraction ϕ: 0.43 (blue), 0.45 (orange), 0.47 (green), 0.49 (red) and 0.51 (purple).

experimental measurements by a power law (coloured straight lines in figure 6):

$$\Sigma_{12} = K\dot{\gamma}^n, \tag{3.1}$$

where K and n are the consistency factor and the shear-thinning index, respectively. Their values resulting from the fits of the experimental data in figure 6 are displayed as functions of ϕ in figure 8. We observe in figure 8(*a*) that K increases with ϕ as expected. This reflects the increase of the viscosity with volume fraction. On the other hand, we observe in figure 8(*b*) that n decreases with ϕ, which accounts for the more pronounced shear-thinning behaviour at large ϕ. One can also note that n is systematically smaller in the case of C_{PS40} at a given ϕ, which reflects the more pronounced shear-thinning behaviour for the suspension made of crushed particles. More precisely, we observe that the relative variation of n over the range of studied ϕ is roughly twice as large for C_{PS40} than for S_{PS40} ($\Delta n/\langle n\rangle \sim 0.2$ for crushed particles whereas $\Delta n/\langle n\rangle \sim 0.1$ for spheres). Regarding the consistency factor, K, it is interesting to see that apparently $K^{C_{PS40}} \approx K^{S_{PS40}}$ at a given ϕ. However, any further interpretation of this comparison in K can be difficult since its units are not exactly the same between the two suspensions because $n^{C_{PS40}} \neq n^{S_{PS40}}$ ($[K] = \mathrm{Pa\ s}^n$).

From figures 6 and 8, it can be seen that the more pronounced shear-thinning behaviour which characterises the suspension C_{PS40} compared with the same suspension made of spheres (S_{PS40}) results from the observations that $\eta_r^{C_{PS40}} \approx \eta_r^{S_{PS40}}$ at large Σ_{12} whereas $\eta_r^{C_{PS40}} > \eta_r^{S_{PS40}}$ at small Σ_{12}.

To conclude this section, we discuss why we have not considered the existence of a yield stress for either suspension. It is true that it is more relevant to characterise the rheological behaviour for some non-Brownian suspensions by using the Herschel–Bulkley (H-B) law:

$$\Sigma_{12} = \tau_c + K\dot{\gamma}^n \tag{3.2}$$

instead of (3.1). According to the literature (Pantina & Furst 2005; Guy *et al.* 2018; Richards *et al.* 2020), it is known that the existence of a yield stress, τ_c, may be caused by

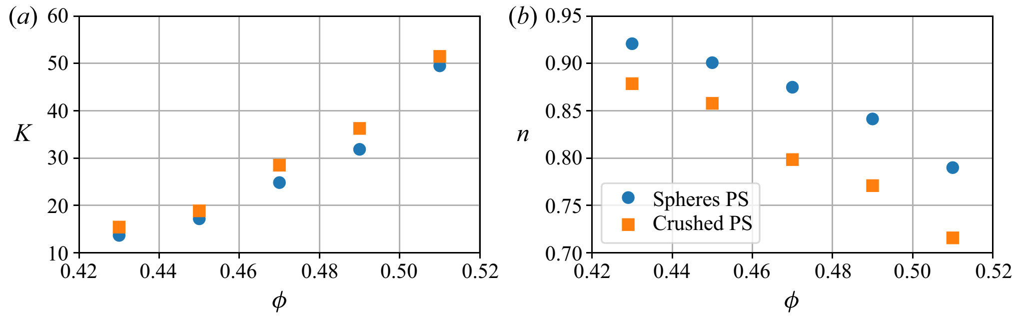

Figure 8. Variation of (*a*) the consistency factor K and (*b*) the shear-thinning index n with solid volume fraction ϕ for the suspensions S_{PS40} made of spherical PS particles (blue discs) and C_{PS40} made of crushed PS particles (orange squares), deduced from (3.1).

the presence of weak adhesive forces between solid particles which would lead to particle aggregation. Thus, the value of τ_c may be understood as the minimum stress required to break these aggregates. Furthermore, it is expected that the crushed particles, which have some flat faces, favour Van der Waals interactions since they offer a much larger contacting surface between particles compared with spheres, leading to a higher yield stress. In view of this, we have also fitted our experimental measurements in figure 6 by (3.2). The results have shown that the impact of the third fitting parameter τ_c on K and n is negligible, since we found $\tau_c < 1$ Pa for both suspensions and all explored ϕ. For S_{PS40}, one can note that this is in good agreement with the works of Le *et al.* (2023) who measured $\tau_c = 0.3$ Pa for a very dense suspension made of PS beads having a size of 40 µm and concentration $\phi = 0.55$ in a silicone oil (the same system as studied in the present paper). The largest volume fraction studied in the present work being $\phi = 0.51$, one can expect that the values of τ_c for S_{PS40} are even smaller than this value within the range of studied ϕ. Thus, we can advance with enough confidence that the minimum applied shear stress in our study ($\Sigma_{12} = 5$ Pa) is at least 10 times larger than τ_c for S_{PS40} and C_{PS40}. We confirm by some measurements from the shear-reversal experiments that adhesive forces do not play a significant role in the rheological behaviour of the studied suspensions within the applied range of shear stress Σ_{12}.

3.1.2. *A stress-dependent jamming volume fraction*

We want to recall that the shear-thinning regime observed for a frictional non-Brownian suspension is common and has already been observed extensively in the literature for suspensions made of spheres (Gadala-Maria & Acrivos 1980; Zarraga *et al.* 2000; Dbouk *et al.* 2013; Vázquez-Quesada *et al.* 2016, 2017) or even facetted (sugar) particles (Blanc *et al.* 2018). As explained in the introduction of the present paper, the physical origin of this complex behaviour remains an open question. Some recent works, including an experimental study from Chatté *et al.* (2018) and numerical simulations from Lobry *et al.* (2019), have demonstrated that the shear-thinning behaviour for frictional spheres could come from a decay of the sliding friction coefficient, μ_s, when the shear stress, Σ_{12}, increases, which induces an increase of the jamming volume fraction, ϕ_m (Wildemuth & Williams 1984; Zhou, Uhlherr & Luo 1995; Blanc *et al.* 2018; Lobry *et al.* 2019; Gilbert *et al.* 2022). The introduction of a stress-dependent jamming fraction $\phi_m(\Sigma_{12})$ is thus very useful to describe accurately the complex rheological behaviour of a suspension. Figure 9 displays the evolution of η_r with ϕ for each applied Σ_{12} (see colour code). The coloured

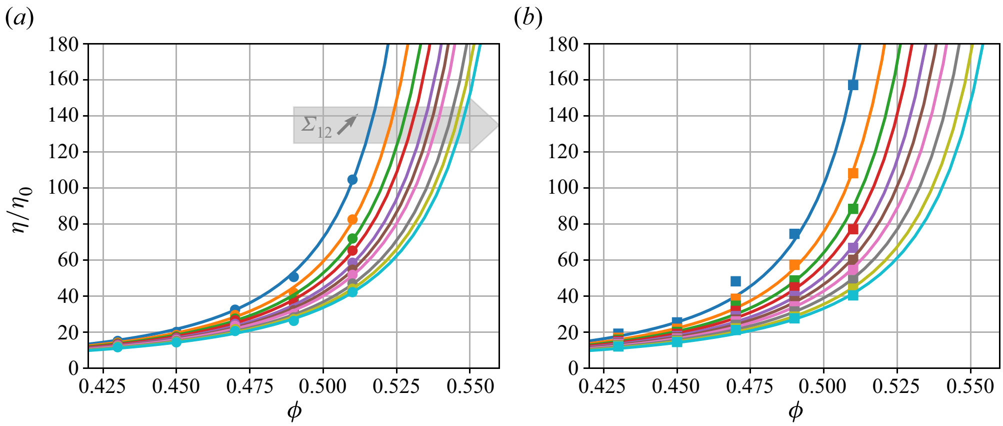

Figure 9. Variation of measured relative steady viscosity η_r with solid volume fraction ϕ for suspensions (*a*) S_{PS40} made of spherical PS and (*b*) C_{PS40} made of crushed PS particles. Each colour labels the applied shear stress Σ_{12}: 5 (blue), 10 (orange), 15 (green), 20 (red), 28 (purple), 36 (brown), 45 (pink), 60 (grey), 80 (yellow) and 100 (cyan). For each given Σ_{12}, the experimental measurements (coloured dot) are fitted by a Maron–Pierce-type law (see (3.3)). The measurements of $\phi_m(\Sigma_{12})$ resulting from these fits are shown in figure 10.

points correspond to the experimental data and, for each applied Σ_{12}, the variation of the reduced viscosity, η_r, with the volume fraction, ϕ, is fitted by a Maron–Pierce-type law:

$$\eta_r = \frac{\alpha_0}{\left(1 - \dfrac{\phi}{\phi_m(\Sigma_{12})}\right)^2}. \tag{3.3}$$

Note that the parameter α_0 in (3.3) is used in order to get an accurate fit of our experimental data. If one were to apply (3.3) over the full range of particle volume fractions, α_0 would need to be 1 in order that $\eta_r = 1$ when $\phi \to 0$. However, this fit only works in the dense regime, typically for $\phi \gtrsim 0.3$ in the case of frictional spherical particles, and hence α_0 can have a value different from 1 in order to describe the variation of η_r with ϕ accurately within this regime (Lobry *et al.* 2019). In our case, a very good fit for each applied shear stress (plotted as coloured lines in figure 9) is obtained for $\alpha_0 = 0.85$ for both suspensions, a value not too far from the one used in the original equation of Maron & Pierce (1956): $\alpha_0 = 1$ when $\phi_m \approx 0.64$. The value chosen here is also in good agreement with the numerical simulations of Lobry *et al.* (2019) who have found that $0.65 \lesssim \alpha_0 \lesssim 1$ when $0 \lesssim \mu_s \lesssim 2$, which are the typical values of μ_s for common materials such as PS (Arshad *et al.* 2021; Le *et al.* 2023), polymethyl methacrylate, glass and rubber. In figure 9(*b*), we can observe that it satisfactorily fits the experimental data for crushed particles.

The good fit obtained with this given value of α_0 for both suspensions is not so surprising as it is known that the values of η_r when $\phi \to \phi_m$ are controlled primarily by the value of ϕ_m (Blanc *et al.* 2018; Lobry *et al.* 2019). Figure 10 displays the variation of ϕ_m with Σ_{12}, determined by (3.3) with $\alpha_0 = 0.85$ for the suspensions S_{PS40} made of PS beads (blue circle) and C_{PS40} made of crushed particles (orange squares). As expected, we observe that ϕ_m increases with Σ_{12} for both suspensions. This increase is larger for C_{PS40} when compared with S_{PS40}, which illustrates the more pronounced shear-thinning behaviour for the suspension made of crushed particles. To be precise, we observe that $\phi_m^{C_{PS40}} < \phi_m^{S_{PS40}}$ within the smaller end of the Σ_{12} range whereas $\phi_m^{C_{PS40}} \approx \phi_m^{S_{PS40}}$ at

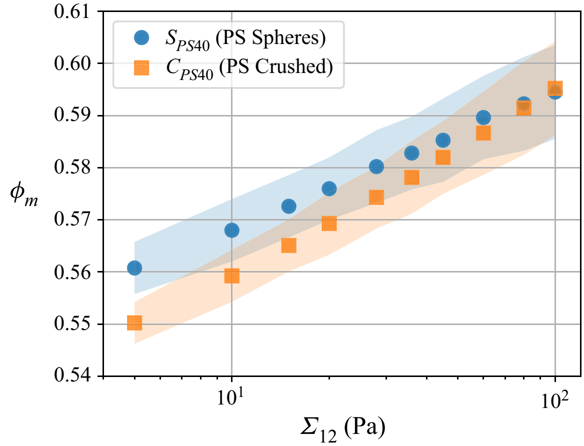

Figure 10. Variation of the jamming fraction ϕ_m with shear stress Σ_{12} for the suspensions S_{PS40} made of spheres PS (blue circle) and C_{PS40} made of crushed PS particles (orange square), deduced from figure 9 and (3.3) with $\alpha_0 = 0.85$. The coloured area for each suspension is related to the possible range of α_0: $0.65 \lesssim \alpha_0 \lesssim 1$.

the largest Σ_{12} values. This mirrors the previous observation made from the viscosity comparison between the two suspensions.

It is easy to understand that the values of ϕ_m determined by (3.3) might depend slightly on the value of α_0, and hence we have also fitted our experimental data of $\eta_r(\phi)$ by (3.3) with the two known extreme values of α_0 (Lobry *et al.* 2019): $\alpha_0 = 0.65$ and $\alpha_0 = 1$ (the corresponding curves are not plotted in figure 9 in order to keep the graph clear). The confidence areas plotted in figure 10 for each suspension represent this influence of α_0 on ϕ_m. Thus, one can observe that the values of ϕ_m for S_{PS40} are between 0.560 ± 0.005 and 0.595 ± 0.009 in very good agreement with Lobry *et al.* (2019), whereas they are between 0.550 ± 0.004 and 0.595 ± 0.009 for C_{PS40}. It is quite satisfying that these values of ϕ_m for both types of suspension are globally in very good agreement with the literature when non-Brownian frictional ($\mu_s \neq 0$) suspensions are considered (Zarraga *et al.* 2000; Ovarlez *et al.* 2006; Boyer *et al.* 2011; Mari *et al.* 2014; Peters *et al.* 2016; Singh *et al.* 2018; Lobry *et al.* 2019; Singh *et al.* 2020). Furthermore, it is noteworthy that the primary observations that the jamming volume fraction ϕ_m is smaller in the case of non-spherical particles at low shear stress whereas the rheological behaviours of non-spherical and spherical particles are characterised by the same ϕ_m at high shear stress is not altered by the value of α_0 within its known range.

The rest of the paper focuses on finding a physical mechanism to explain the observed rheological difference between the suspension made of crushed particles and the suspension made of spheres.

3.2. *Physical origin of the stronger shear-thinning regime for crushed particles*

In this section, we want to understand the physical origin of the higher viscosity in the suspension of crushed particles (C_{PS40}) for small shear stress, as well as the reason that the viscosity of the two types of suspension are similar when Σ_{12} is increased. Since the only difference between the suspensions is the shape of particles present in them, it is obvious that this difference in viscosity is related to it. Two different possible physical origins will be thus investigated. First, we show in § 3.2.1 that it is unlikely that the small remaining adhesion between particles (which is expected to be stronger for the crushed particles at a given shear stress) explains this observation. Second, we discuss in §§ 3.2.2 and 3.2.3 whether changes in viscosity can be explained by a variable sliding friction between particles coupled with a rolling resistance of particles related to the particle shape itself. To end this section, we study in § 3.2.4 the rheological behaviour of the suspensions in a frictionless case in order to confirm some assumptions of the considered model.

3.2.1. *Shear reversal experiments and absence of adhesion*

As mentioned previously in this paper, shear-thinning behaviour of a suspension is common and can have different possible physical origins depending on the studied system (Gadala-Maria & Acrivos 1980; Zarraga *et al.* 2000; Dbouk *et al.* 2013; Vázquez-Quesada *et al.* 2016, 2017; Blanc *et al.* 2018; Chatté *et al.* 2018; Lobry *et al.* 2019; Gilbert *et al.* 2022). One of them is adhesion. Weak adhesive forces exist between solid particles that would lead to particle aggregation. In this scenario, two main features would appear. First, a suspension would exhibit a yield stress τ_c (Brown *et al.* 2010), which may be understood as the minimum stress needed to break these aggregates. Second, they would exhibit shear-thinning behaviour, related to the fact that increasing Σ_{12} would break more and more aggregates, which would produce as a result a decrease in the viscosity of the suspension. Furthermore, this explanation would be suitable to explain the highest viscosity at low Σ_{12} for crushed particles while the viscosity of the two types of suspensions (S_{PS40} and C_{PS40}) would tend to be similar at large Σ_{12}. As already mentioned previously in § 3.1.1, flat surfaces of crushed particles favour particle adhesion. Potential aggregates are then less likely to be destroyed in C_{PS40} than in S_{PS40} when both suspensions are sheared at a given small enough Σ_{12}. This would make C_{PS40} more viscous than S_{PS40} when Σ_{12} is small. In contrast, when $\Sigma_{12} \gg \tau_c$, all the aggregates are destroyed by shear, even in the case of C_{PS40} which then flows similarly to S_{PS40}.

The first flaw in this explanation has already been presented in § 3.1.1. Indeed, we have seen that the smallest value of Σ_{12} that we apply to shear the suspension is at least 10 times larger than τ_c. At $\Sigma_{12} = 10$ Pa (second lowest value of applied shear stress), we have $\Sigma_{12} \gtrsim 20 \times \tau_c$. Yet, a significant difference of viscosity between the two suspensions still remains at large ϕ, which raises doubt that adhesion could be the main physical origin of the stronger shear-thinning for C_{PS40}. For instance, at $\phi = 0.51$ and $\Sigma_{12} = 10$ Pa, $\eta_r = (110 \pm 5)$ Pa s for C_{PS40} whereas $\eta_r = (80 \pm 5)$ Pa s for S_{PS40} (see figure 9), which gives a difference of the order of 30 %. Nevertheless, we understand that this argument about Σ_{12} and τ_c alone is insufficient to support the statement that the adhesion is not mainly responsible for the more pronounced shear-thinning for C_{PS40}. It is indeed very difficult to estimate precisely when the adhesive forces can be neglected only from τ_c. To go further, we have conducted a series of shear-reversal experiments on both types of suspension by following the procedure of Blanc *et al.* (2018).

A shear-reversal experiment may turn out to be very interesting. It is a very basic experiment (the suspension is simply sheared at a given Σ_{12} in a given direction before the flow direction is reversed whereas Σ_{12} is kept constant), characterised by a very specific transient response of η which has been observed in all shear reversal experiments (Gadala-Maria & Acrivos 1980; Blanc *et al.* 2011*a*) and in simulations (Ness & Sun 2016; Peters *et al.* 2016). Figure 11 displays an example of the transient response of η for S_{PS40} (in blue) and C_{PS40} (in orange) at $\Sigma_{12} = 10$ Pa and $\phi = 0.51$. As can be observed, a step-like drop of η occurs just after the shear reversal and the viscosity of the suspension reaches a minimum value, η_{min}, at a strain $\gamma = \gamma_{min}$ ($\gamma = 0$ corresponds to the moment of reversal). This drop is then followed by a rebound of the viscosity which reaches the steady value,

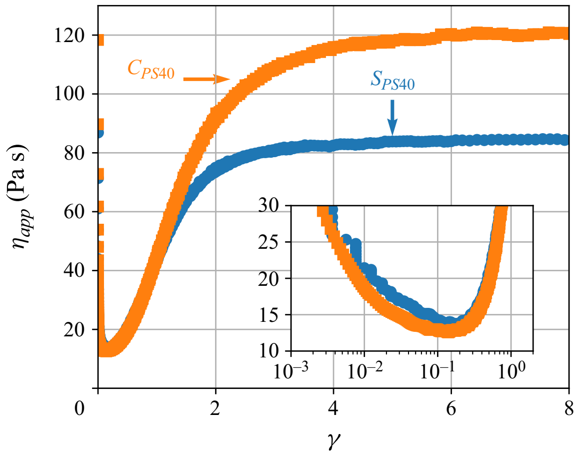

Figure 11. Example of transient viscosity response as a function of the accumulated strain γ during a shear reversal experiment for S_{PS40} (in blue) and C_{PS40} (in orange) with $\Sigma_{12} = 10$ Pa and $\phi = 0.51$. $\gamma = 0$ corresponds to the moment when the flow is reversed. Inset: Enlarged view to better visualise the minimum value of viscosity, η_{min} reached during the transient when $\gamma = \gamma_{min}$.

$\eta_s = \eta_0\eta_r$, it had before the shear reversal, over an accumulated strain, γ, roughly equal to $\gamma_s \sim 10$. Interestingly, the numerical simulations from Ness & Sun (2016) and Peters *et al.* (2016) have shown that the hydrodynamic and contact contribution to the viscosity, denoted respectively η^H and η^C, are connected directly to the values of η and η_{min}. More precisely, with $\eta_s = \eta^H + \eta^C$, Peters *et al.* (2016) have numerically shown in the case of a non-Brownian suspension made of (frictional or frictionless) beads the following relations:

$$\eta^C = \frac{\eta_s - \eta_{min}}{0.85/\eta_0} \quad \text{and} \quad \eta^H = \frac{\eta_{min} - 0.15\eta_s}{0.85/\eta_0}. \tag{3.4a,b}$$

Roughly, $\eta^H \sim \eta_{min}/\eta_0$ and $\eta^C \sim (\eta_s - \eta_{min})/\eta_0$. We refer readers to the numerical work of Peters *et al.* (2016) to better understand the physical origin of this result. In brief, the particles in contact tend to separate when the shear is reversed. The microstructure of the suspension is thus broken, which induces the drop of the viscosity. Progressively, the microstructure of the suspension is then rebuilt (mirroring the microstructure before the shear reversal since the flow direction has been reversed), which induces the rebound of η to its steady value.

In the present study, the transient viscosity induced by a shear reversal can be very interesting because, if a stress-dependent particle aggregation occurs, then it should also affect the values of η_{min} and the characteristic strains, γ. Notably, Gilbert (2021) has studied the rheology of a non-Brownian frictional suspension composed of homemade soft PDMS particles (Young modulus, $E_{PDMS} = 1.8$ MPa $\ll E_{PS} \sim 3$ GPa) suspended in Span 80 (Newtonian liquid). By using the JKR theory (Johnson, Kendall & Roberts 1971), the author has observed for this suspension that adhesion plays a role if $\Sigma_{12} \lesssim \tau_a \approx 10$ Pa. By doing shear reversal experiments, he has then shown (see figures 86-2 of Gilbert 2021) that $\eta_{min}^{\Sigma_{12}<\tau_a} \gg \eta_{min}^{\Sigma_{12}>\tau_a}$, and that the characteristic deformation of the transient response for a shear reversal, γ_s, was much larger than 10 ($\gamma_s \sim 50$ for $\phi = 0.4$ and $\Sigma_{12} = \tau_a$ in the case of his suspension).

Figure 12 displays the experimental measurements (coloured symbols) of η_{min}/η_0 within the studied range of Σ_{12} for (*a*) S_{PS40} and (*b*) C_{PS40}, and one can see it is not similar to what has been observed by Gilbert (2021) for a non-Brownian suspension made of

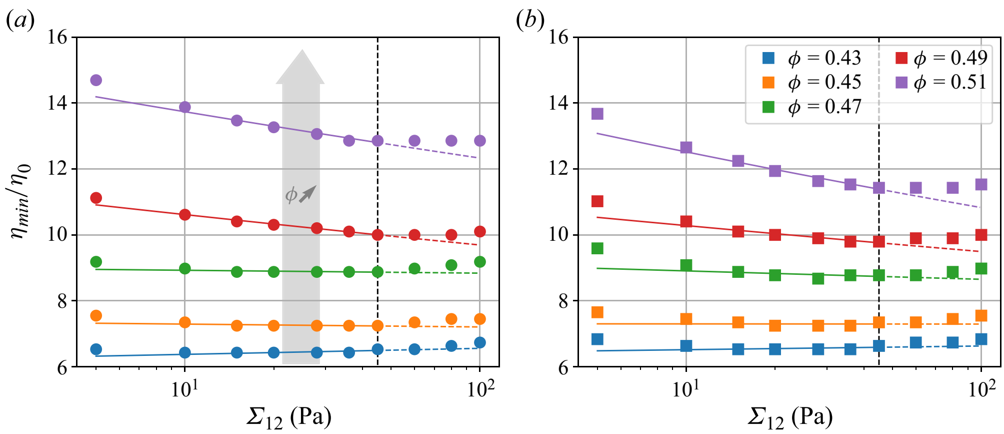

Figure 12. Variation of the measured relative minimum value of the viscosity, η_{min}/η_0, with applied shear stress Σ_{12} for (*a*) the suspension made of spherical PS and (*b*) the suspension made of crushed PS particles. The colour code labels the solid volume fraction ϕ of the suspension in the same way as in figure 6. For each given ϕ, the experimental measurements (coloured symbols) for $\Sigma_{12} \leqslant 45$ Pa are fitted by a power law (coloured straight line): $\Sigma_{12} = K_{min} \times \dot{\gamma}^{\nu_{min}}$ with $\dot{\gamma} = \Sigma_{12}/\eta_{min}$. The parameters resulting from these fits are shown in figure 13.

adhesive beads. First, $\eta_{min}^{C_{PS40}} \approx \eta_{min}^{S_{PS40}}$ at a given Σ_{12} and a given ϕ. Second, η_{min} is weakly dependent on Σ_{12} for a given ϕ in the studied range of applied shear stress. Thus, it is likely that $\Sigma_{12} \gg \tau_a$ for both suspensions in the present study and that adhesion can then be neglected. We also want to underline that, based on (3.4*a*,*b*), we can determine $\eta^H \approx$ 5–6 for S_{PS40} concentrated at 45 % from the experimental data (roughly independent of Σ_{12}), which is in very good agreement with numerical simulations from Gallier *et al.* (2014) which shows $\eta^H \approx \eta_\infty \approx$ 5–6 for a non-Brownian viscous suspensions of (frictionless or frictional) spheres at $\phi = 0.45$. Here η_∞ is the high-frequency dynamic viscosity (Van der Werff & De Kruif 1989).

Note that, in figure 12, the experimental data for η_{min} of each suspension for $\Sigma_{12} \leqslant 45$ Pa have been then fitted by a power law, based on (3.1) where now $K \equiv K_{min}$ and $n \equiv n_{min}$, to quantify these observations of η_{min}. The fitting parameters K_{min} and n_{min} resulting from this fit are presented in figure 13. The upper limit for the shear stress considered here for the fit ($\Sigma_{12}^{max} = 45$ Pa) is imposed due to the poor resolution of the measurement of η_{min} when $\Sigma_{12} > \Sigma_{12}^{max}$. Thus, the apparent plateau of η_{min} observed at large Σ_{12} has no physical meaning. It is an experimental artifact. Therefore, one can clearly see in figure 13 that η_{min} for the suspensions S_{PS40} and C_{PS40} are characterised by the same rheology, as we observe that both K_{min} and n_{min} are independent of the considered suspension. In addition, S_{PS40} and C_{PS40} are both characterised by a Newtonian behaviour when $\eta = \eta_{min}$: $0.94 \lesssim n_{min} \lesssim 1$ for both suspensions, when $0.43 \leqslant \phi \leqslant 0.51$ and $5 \leqslant \Sigma_{12} \leqslant 100$ Pa. Moreover, the η_{min} results indicate that hydrodynamic interactions are not significantly affected by particle shape.

Figure 14 displays the experimental values of characteristic strains, γ_{min} (open symbols) and $\gamma_{0.5}$ (closed symbols) for the suspension made of PS spheres (blue) and that made of crushed particles (orange), as a function of ϕ when $\Sigma_{12} = 10$ Pa. Whereas γ_{min} corresponds to the accumulated strain from the moment of shear reversal to when $\eta = \eta_{min}$, $\gamma_{0.5}$ is defined as the accumulated strain from the minimum state ($\eta = \eta_{min}$)

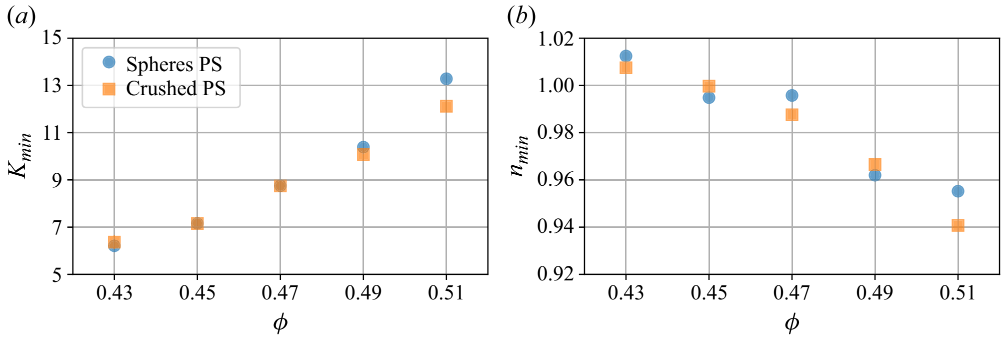

Figure 13. Variation of (*a*) the consistency factor, denoted K_{min}, and (*b*) the shear-thinning index, denoted n_{min}, with the solid volume fraction ϕ for the suspension made of spherical PS particles (blue discs) and the suspension made of crushed PS particles (orange squares), when $\eta = \eta_{min}$ and $\Sigma_{12} \leqslant 45$ Pa.

to the moment when the viscosity has recovered 50 % of its reversal-induced deficit:

$$\eta(\gamma_{0.5}) = \eta_{min} + 0.5 \times (\eta_s - \eta_{min}) . \tag{3.5}$$

The uncertainties of the experimental measurements for the characteristic strains are estimated at $\pm 5 \times 10^{-2}$. The experimental data are also compared with numerical (Pine *et al.* 2005; Peters *et al.* 2016) and experimental (Pine *et al.* 2005) results from the literature. We recall that Pine *et al.* (2005) have shown that a particle in a non-Brownian suspension subjected to oscillatory shear flow returns to its initial position at each oscillatory cycle consistent with Stokes flow reversibility as long as the strain amplitude does not exceed a critical value, denoted γ_c. As explained by Peters *et al.* (2016), $\gamma_{0.5}$ corresponds to the strain necessary for spherical particles to form a significant amount of solid contacts which would then lead to displacements that violate Stokes flow reversibility.

One can observe that γ_{min} decreases with ϕ for both suspensions and that $\gamma_{min}^{C_{PS40}} \sim \gamma_{min}^{S_{PS40}}$ for a given ϕ. A closer examination shows that $\gamma_{min}^{C_{PS40}}$ is nearly equal to $\gamma_{min}^{S_{PS40}}$ at the highest volume fraction ($\phi = 0.51$) whereas it is smaller than $\gamma_{min}^{S_{PS40}}$ at smaller volume fractions with the largest difference occurring $\phi = 0.43$, the lowest volume fraction studied. Furthermore, one can note that the experimental data are well-predicted by the simulations from Peters *et al.* (2016), conducted on a non-Brownian suspension of frictional spheres, characterised by a combination of a sliding friction coefficient, $0 \leqslant \mu_s \leqslant 1$, and a relative roughness height, $h_r/d = 10^{-2}$.

Analogous to γ_{min}, we observe that $\gamma_{0.5}$ decreases when ϕ increases, which is in good agreement with the literature. In addition, the experimental values for S_{PS40} at $\Sigma_{12} = 10$ Pa (filled blue discs) are well-captured by the numerical simulations from Peters *et al.* (2016) ($\mu_s = 0.5$, $h_r/d = 10^{-2}$). One can also note that $\gamma_{0.5}^{C_{PS40}} \gtrsim \gamma_{0.5}^{S_{PS40}}$ for a given ϕ even though both are still of the same order and follow the same trend. This slight difference is interesting for two different reasons. First, as we have seen from the work of Gilbert (2021), having $\gamma_{0.5}^{C_{PS40}} \sim \gamma_{0.5}^{S_{PS40}}$ (and $\gamma_s \sim 10$ as can be observed in figure 11) is consistent with the inference that adhesion forces do not play a predominant role in the rheology of C_{PS40} compared with S_{PS40}, within the applied range of Σ_{12}. Second, Peters *et al.* (2016) have explained that the force network is reestablished over a typical strain equal to $\gamma_{0.5}$ during a shear reversal experiment. According to this assertion, it would be a little harder for the particles in C_{PS40} to rearrange during the transient in order to rebuild the microstructure

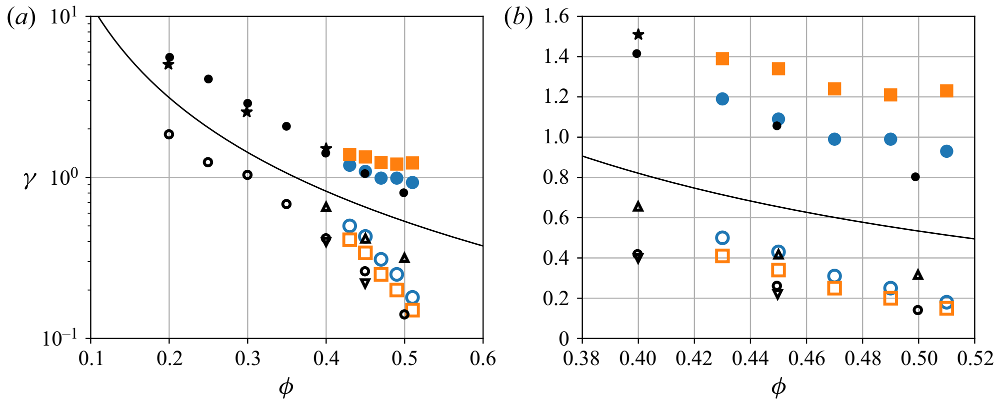

Figure 14. Characteristic strains γ_{min} for the minimum viscosity (open symbols) and $\gamma_{0.5}$ for the partial recovery (filled symbol) as a function of volume fraction ϕ. The graph on the right is just an enlarged view of the left graph. The experimental measurements ($\Sigma_{12} = 10$ Pa) from this study are represented for the suspensions S_{PS40} (blue discs) and C_{PS40} (orange squares). From the literature, Peters *et al.* (2016) have performed several numerical simulations to study the influence of the sliding friction coefficient μ_s and the relative roughness h_r/d on γ_{min} and $\gamma_{0.5}$. Some of their results are also plotted (black symbols) on the graph for $h_r/d = 10^{-2}$ (empty symbols for γ_{min} and filled symbols for $\gamma_{0.5}$): (△) $\mu_s = 0$; (○) $\mu_s = 0.5$; (∇) $\mu_s = 1$. Some experimental measurements (⋆) from Pine *et al.* (2005) of the critical strain γ_c for which irreversibility occurs are also plotted, as well as the power law (—) resulting from their numerical simulations: $\gamma_c = 0.14\phi^{-1.93}$.

leading to contact forces (see the works from Peters *et al.* (2016) for details on the physical mechanism). We think this is related to the shape-induced rolling resistance and it could be interesting to study it using numerical simulations, because shear reversal gives access to the separate hydrodynamic and contact contributions to the stress. More generally, Peters *et al.* (2016) have studied the influence of μ_s and h_r/a on the values of characteristic strains and we think it could be interesting to also quantify the role played by μ_r, if any, in the transient of a shear-reversal experiment.

3.2.2. *Variable sliding friction coefficient*

In the previous section, we have seen that adhesion cannot account for the shear-thinning behaviour of the two suspensions and that there is no evidence from shear reversal experiments of stronger adhesion in C_{PS40} than S_{PS40}. In this section, we show that, unlike adhesion, a variable sliding friction model allows us to explain the shear-thinning behaviour of the suspensions.

From the numerical works of Mari *et al.* (2014) and Gallier *et al.* (2014), it is well known that the jamming volume fraction, ϕ_m, is strongly dependant on the sliding friction coefficient, μ_s. In addition, as presented in the introduction of the present paper, the recent literature (Chatté *et al.* 2018; Lobry *et al.* 2019; Arshad *et al.* 2021; Le *et al.* 2023) relates the shear-thinning behaviour of a non-Brownian frictional suspension to a decay of μ_s when the normal force F_N between particles (directly proportional to Σ_{12}) increases:

$$\mu_s = \mu_s^\infty \times \coth\left[\mu_s^\infty \left(\frac{\Sigma_{12}}{\Sigma_c}\right)^m\right] \quad \text{with } \mu_s \xrightarrow{\Sigma_{12}\to\infty} \mu_s^\infty. \tag{3.6}$$

We recall that Σ_c is a critical value which characterises the elastoplastic transition of asperities deformation (Lobry *et al.* 2019) and μ_s^∞ is the constant value reached by μ_s when $\Sigma_{12} \gg \Sigma_c$. As for the exponent m, its value is directly related to the fact that

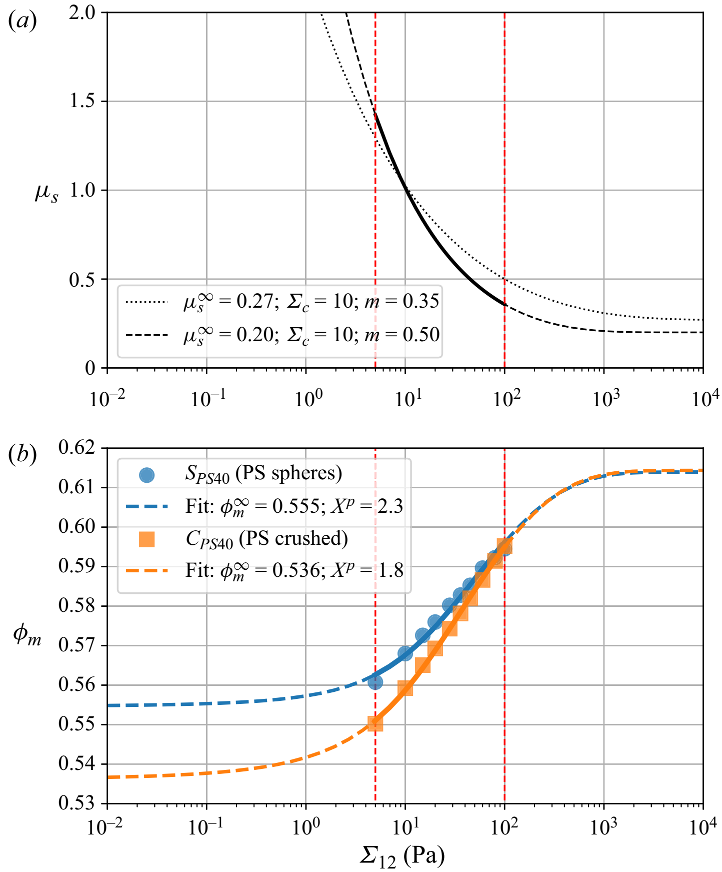

Figure 15. (a) Variation of the sliding friction coefficient μ_s with Σ_{12} (see (3.6)) as computed by Brizmer *et al.* (2007) and Lobry *et al.* (2019) ($\cdots$) and the variation used to fit the experimental data $\phi_m(\Sigma_{12})$ (——). The solid part of the curve corresponds to the experimentally studied range of Σ_{12}. (b) Jamming volume fraction ϕ_m as function of shear stress Σ_{12}. The experimental measurements for S_{PS40} (blue discs) and C_{PS40} (orange squares) are fitted by the model obtained by combining (3.6) and (3.7), where $\mu_s^\infty = 0.2$, $\Sigma_c = 10$ Pa, $m = 0.5$ and $\phi_m^0 = 0.65$. Here ϕ_m^∞ and X^p are free parameters. The best fit gives $\phi_m = 0.555$ and $X^p = 2.3$ in the case of S_{PS40}. For C_{PS40}, we determined $\phi_m = 0.536$ and $X^p = 1.8$. The two vertical dashed red straight lines on each graph delimit the range of Σ_{12} explored experimentally.

the model (Lobry *et al.* 2019) considers that the contact between two particles occurs at only one or two asperities (mono-asperity contact) and that the particle asperities are supposed to be close to hemispheres (for which $m \sim 1/3$, Brizmer *et al.* 2007). Recent AFM measurements performed on PS beads ($d \approx 40$ µm) suspended in an aqueous liquid (Arshad *et al.* 2021) or in silicone oil (Le *et al.* 2023) have given $\mu^\infty \approx 0.2$, $\Sigma_c \approx 10$ Pa and $m \approx 0.5$. Figure 15(a) displays the variation of μ_s with Σ_{12} based on these values (——).

Our main assumption is that (3.6) can describe the variation of μ_s with Σ_{12} in both suspensions. In addition to the form of the function, we assume that the values of μ_s^∞, Σ_c and m are also identical for both types of particles: spheres and crushed. We understand that this statement is critical but several arguments tend to support it. We recall that sliding friction should depend on the local interaction of two surfaces. In the present study, the same PS particles (in size and material) constitute the two studied suspensions and, even though the crushing process does change the radii of curvature of particles in some places, we assume that it does not significantly affect the topology of the asperities. Thus, as considered from Peters *et al.* (2016) for spheres, we assume that the solid contact between particles occurs through only a few asperities even to the crushed particles in C_{PS40}. In this scenario, the value of m determined by Arshad *et al.* (2021) and Le *et al.* (2023) for PS spherical particles ($m \approx 0.5$) can be applied for the crushed ones. Moreover, the values of μ_s^{∞} and Σ_c determined for PS beads ($\mu_{\infty} \approx 0.2$ and $\Sigma_c \approx 10$ Pa) by Arshad *et al.* (2021) and Le *et al.* (2023), depending on the properties of the solid particle material (Young's modulus E, Poisson's ratio ν, yield strength Y_0) and asperity height h_r, can also be kept the same for the crushed PS particles. We want to underline that the assumption that $\mu_s^{C_{PS40}}(\Sigma_{12}) \approx \mu_s^{S_{PS40}}(\Sigma_{12})$ is also consistent with the results displayed in figure 14 for the characteristic strain, γ_{min}. Indeed, Peters *et al.* (2016) have shown the role played by μ_s on γ_{min}, and the experimental data from the present study tend to show that the values of μ_s are between 0 and 1 for the studied suspensions and are very similar between the two.

Lobry *et al.* (2019) have proposed the following phenomenological function $\phi_m(\mu_s)$ relating the jamming volume fraction to the sliding friction coefficient:

$$\phi_m = \phi_m^{\infty} + \left(\phi_m^0 - \phi_m^{\infty}\right)\left[\frac{\exp(-X^p \operatorname{atan}(\mu_s)) - \exp(-\pi X^p/2)}{1 - \exp(-\pi X^p/2)}\right], \tag{3.7}$$

where ϕ_m^{∞} and ϕ_m^0 are specific values of ϕ_m when the particles cannot slide ($\mu_s \xrightarrow{\Sigma_{12}\to 0} \infty$) and when the suspension is frictionless ($\mu_s \to 0$), respectively. The expression contains a fitting parameter X^p. Figure 15(*b*) redisplays the variation of the jamming volume fraction, ϕ_m, with shear stress, Σ_{12} (already shown in figure 10). In this new figure, the experimental data (represented as blue discs for S_{PS40} and orange squares for C_{PS40}) are fitted by the model described by (3.6) and (3.7). Additionally, ϕ_m^{∞} and X^p are left as free parameters while ϕ_m^0 is set equal to 0.65, in good agreement with the literature when the frictionless ($\mu_s = 0$) regime is considered (Gallier *et al.* 2014; Mari *et al.* 2014; Gallier, Peters & Lobry 2018; Singh *et al.* 2018; Le *et al.* 2023). We show later in the present paper (in § 3.2.4) that it is also in very good agreement with the rheology of S_{PS40} and C_{PS40} sheared in the frictionless regime.

We observe that the experimental data are well-predicted by the model within the experimentally explored range of shear stress ($\Sigma_{12} \in [5\text{–}100]$ Pa, coloured solid lines in figure 15*b*). By coupling figures 15(*a*) and 15(*b*), one can note that $\phi_m^{S_{PS40}} \approx (0.585 \pm 0.008)$ when $\mu_s \approx 0.5$ ($\Sigma_{12} \sim 45$ Pa) and $\phi_m^{S_{PS40}} = (0.568 \pm 0.006)$ when $\mu_s = 1$ ($\Sigma_{12} \sim 10$ Pa) for the suspension made of spheres, which is in quite good agreement with numerical simulations from the literature. For instance, Peters *et al.* (2016) and Gallier *et al.* (2018) found $\phi_m \approx 0.59$ and $\phi_m \approx 0.58$, respectively, when $\mu_s = 0.5$. The numerical simulations of Mari *et al.* (2014) and the ones from Peters *et al.* (2016) predict $\phi_m \approx 0.58$ and $\phi_m \approx 0.56$ for $\mu_s = 1$, respectively.

Then, one can observe in figure 15(*b*) that the variation of ϕ_m with Σ_{12} deduced from the fit exhibits two plateaus (−−), each located at extreme values of shear stress: the first when $\Sigma_{12} \lesssim 10^{-1}$ Pa and the second when $\Sigma_{12} \gtrsim 10^3$ Pa. According to (3.6) (Lobry *et al.* 2019), the plateau when $\Sigma_{12} \to +\infty$ is due to the saturation of μ_s (plastic regime) when $\Sigma_{12}/\Sigma_c \gg 1$ (see figure 15*a*). The other plateau predicted by the fit when $\Sigma_{12} \to 0$ is explained by the weak influence of μ_s on the values of ϕ_m when μ_s is larger than 1 or 2, as demonstrated by the numerical works of Mari *et al.* (2014), Peters *et al.* (2016) and Lobry *et al.* (2019).

In figure 15(*b*), the function $\phi_m(\Sigma_{12})$ deduced from the fit is then characterised by:

(i) $\phi_m \xrightarrow[\mu_s\to\infty]{\Sigma_{12}\to 0} \phi_m^\infty = (0.555 \pm 0.005)$ for S_{PS40} and $\phi_m^\infty = (0.536 \pm 0.004)$ for C_{PS40};

(ii) $\phi_m \xrightarrow[\mu_s\to 0.2]{\Sigma_{12}\to \infty} \phi_m^{0.2} = (0.61 \pm 0.01)$ for S_{PS40} and C_{PS40}.

Note that the estimated values of ϕ_m^∞ and $\phi_m^{0.2}$ for S_{PS40} are in very good agreement with the literature (Fernandez *et al.* 2013; Gallier *et al.* 2014; Mari *et al.* 2014; Peters *et al.* 2016; Lobry *et al.* 2019; Le *et al.* 2023). Mari *et al.* (2014) and Lobry *et al.* (2019) determined $\phi_m \approx 0.56$ and $\phi_m \approx 0.546$ when $\mu_s \to +\infty$, respectively, whereas Le *et al.* (2023) obtained $\phi_m^\infty \approx 0.55$ by studying experimentally the same suspension as S_{PS40}. Peters *et al.* (2016) found $\phi_m \approx 0.61$ when $\mu_s = 0.3$ and Lobry *et al.* (2019) determined $\phi_m \xrightarrow[\mu_s\to 0.27]{\Sigma_{12}\to \infty} \phi_m^{0.27} = 0.625$. Regarding C_{PS40}, one can observe that

$\phi_m^\infty|_{C_{PS40}} < \phi_m^\infty|_{S_{PS40}}$ and $\phi_m^{0.2}|_{C_{PS40}} \approx \phi_m^{0.2}|_{S_{PS40}}$, as expected.

To sum up, we have observed by fitting the experimental data $\phi_m(\Sigma_{12})$ by (3.6) and (3.7) that the shear thinning behaviour of the two studied suspensions (S_{PS40} and C_{PS40}) is induced by the same variable friction law, $\mu_s(\Sigma_{12})$. The main difference between the two is in ϕ_m^∞, whose value is smaller in the case of globular/crushed PS particles compared with the PS spheres. One can note that $X^p|_{C_{PS40}} \sim X^p|_{S_{PS40}} \sim 2$, which supports the statement about the sliding friction being the same for the two types of particles. Moreover, $X^p|_{S_{PS40}} \approx 2.3$ is a value which is in good agreement with the literature (Lobry *et al.* 2019; Arshad *et al.* 2021; Le *et al.* 2023).

3.2.3. *Geometry-related rolling resistance*

A decade ago, Estrada *et al.* (2008, 2011) have simulated rolling regular polygons and shown that the stress was the same as discs (with the same ϕ) equipped with a rolling friction coefficient, μ_r (see the schema in figure 2). This would then mean that the geometric effect is a rolling resistance which, in the case of equivalent discs, can be obtained with a μ_r.

More recently, in the frame of a study characterising the shear-thickening behaviour of suspensions made of hard spheres (for which μ_s is kept constant), Singh *et al.* (2020) have numerically studied the role of torque-activated (or stress-activated) rolling resistance, which can be simply induced by the 'rough' particle shape of particles in real-life suspensions. Note that adhesive surfaces can also induce a resistance to rolling motion but we eliminated this physical origin in § 3.2.1. To this aim, the authors have simulated spherical particles with a rolling resistance characterised by a rolling friction coefficient, μ_r. Singh *et al.* (2020) have then studied the role played by different combinations of μ_r and μ_s in determining the value of the jamming volume fraction, ϕ_m. As shown in figure 16, which displays their result, Singh *et al.* (2020) demonstrated interestingly on the one hand that ϕ_m depends weakly on μ_r when μ_s is small enough (typically, $\mu_s \lesssim 0.35$). For instance, their results show that ϕ_m decreases from 0.62 to 0.60 when μ_r increases from 10^{-3} (vanishing rolling resistance) to 10 (extremely strong rolling resistance), and $\mu_s = 0.2$ (see the blue curve in figure 16). Note that we determined in the present work: $\phi_m = 0.61 \pm 0.01$ when $\mu_s = 0.2$ (see figure 15), which is in very good agreement with this observation. On the other hand, Singh *et al.* (2020) have predicted that ϕ_m is strongly dependent of μ_r when $\mu_s \gtrsim 0.5$. For instance, within the same range of rolling friction coefficient ($\mu_r \in [10^{-3} - 10]$), the authors showed that ϕ_m decreases from 0.57 to 0.36 when $\mu_s = 10$ (see the purple curve in figure 16). Typically, this corresponds to the case where sliding is prevented and only rotation can occur ($\mu_r \ll \mu_s \rightarrow \infty$). In the frame of the present study, this latter result from the literature (Singh *et al.* 2020) is very interesting since, based on the assumption that $\mu_r|_{C_{PS40}} > \mu_r|_{S_{PS40}}$, it can explain the main observation obtained in the previous section: $\phi_m^{\infty}|_{C_{PS40}} < \phi_m^{\infty}|_{S_{PS40}}$ and $\phi_m^{0.2}|_{C_{PS40}} \approx \phi_m^{0.2}|_{S_{PS40}}$. To go further, we plotted in figure 17 the variation of ϕ_m with μ_s, determined by our experimental data in the case of the suspensions S_{PS40} (blue solid line) made of spherical particles and C_{PS40} (orange dashed line) made of crushed particles. We compared these two different variations with the numerical simulations from Singh *et al.* (2020) for suspensions of spheres with two values of the rolling friction coefficient $\mu_r = 0.03$, and $\mu_r = 0.10$ (i.e. the two values of μ_r that we determined in figure 16 with the corresponding value of ϕ_m^{∞} for the two suspensions). One can observe very good agreement between our experimental results and the numerical simulations from Singh *et al.* (2020), which tends to confirm the assessment already formulated by Estrada *et al.* (2008, 2011) that the non-spherical globular particles can be approximated as spheres as long as the effect of their shape is reflected by a rolling resistance, characterised by μ_r. In the case of the rheological measurements, it is then captured by the value of ϕ_m^{∞}.

To sum up, the rheology of the suspensions (S_{PS40} and/or C_{PS40}) is solely determined by μ_r (induced by the non-spherical particle shape) when $\phi_m \rightarrow \phi_m^{\infty}$ ($\mu_s \xrightarrow{\Sigma_{12}\rightarrow 0} \infty$), whereas it is nearly independent of shape when $\phi_m \rightarrow \phi_m^{0.2}$ ($\mu_s \xrightarrow{\Sigma_{12}\rightarrow \infty} \mu_s^{\infty} = 0.2$) or $\phi_m \rightarrow \phi_m^{0}$ ($\mu_s \rightarrow 0$). Estrada *et al.* (2008) have indeed demonstrated in the frame of a numerical study on granular material that the dominant mode of relative motion at the contacts (sliding or rolling) is that which minimises the coefficient of internal friction. This simply means that the particles prefer rolling if $\mu_r \ll \mu_s$ or sliding if $\mu_r \gg \mu_s$. The case where $\mu_r \sim \mu_s$ is obviously more complex since it involves rolling and sliding motion at the same time. Thus, by considering the most extreme case where $\mu_s = 10$ in figure 16 (rolling mode) and having deduced the values of ϕ_m^{∞} for each type of suspension (see § 3.2.2), a value of the rolling friction coefficient $\mu_r^{\phi_m^{\infty}}$ for each suspension can be predicted from the rheological measurements: $\mu_r^{\phi_m^{\infty}}|_{S_{PS40}} = 0.03 \pm 0.02$ and $\mu_r^{\phi_m^{\infty}}|_{C_{PS40}} = 0.10 \pm 0.01$. Note that the uncertainty in $\mu_r^{\phi_m^{\infty}}$ for each suspension is due to the uncertainty in the value of ϕ_m^{∞} related to the possible range of α_0 (see (3.3)).

3.2.4. *Frictionless suspensions made with the same particles*

We have briefly studied the rheology of the frictionless case ($\mu_s = 0$) of the two suspensions studied in the present paper, by dispersing the same PS particles present in S_{PS40} and C_{PS40} in an aqueous solution, labelled $AQ0$, and shearing the suspensions in a vane tool geometry. The aqueous solution is a mixture of deionised water with a small amount (less than 3wt%) of Triton-X-100 (surfactant, Sigma Aldrich) and sodium iodide. We encourage the reader to see the supplementary material of Madraki *et al.* (2020) for more details about this experimental procedure. Furthermore, the critical normal load f_N^C (occurrence of the frictionless–frictional transition) has been measured by AFM measurements by Madraki *et al.* (2020) for PS beads ($d \approx 140$ µm) in this aqueous solution $AQ0$. The authors found $f_N^C = (12 \pm 4)$ µN, which gives $\sigma_{in}^{fft} \approx 0.3 \times f_N^C/(6\pi a^2) \sim 40$ Pa (Mari *et al.* 2014) for this type of suspension (PS beads in $AQ0$).

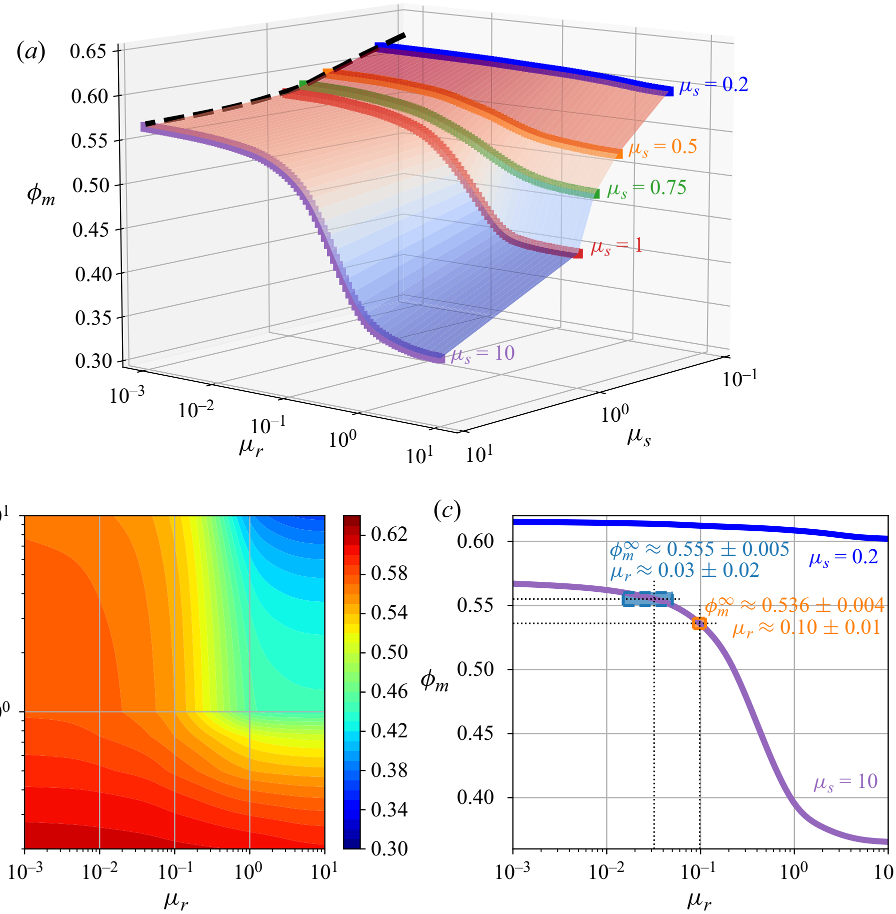

Figure 16. The jamming volume fraction ϕ_m as a function of the sliding friction coefficient, μ_s, and rolling friction coefficient, μ_r, as computed by Singh *et al.* (2020). Their data can be obtained at: https://acdc.alcf.anl.gov/mdf/detail/singh_rolling_friction_prl_2020_v1.4/. Bottom right: Variation of ϕ_m with μ_r for $\mu_s = 0.2$ (blue) and $\mu_s = 10$ (purple). The latter allows one to predict the values of μ_r for S_{PS40} and C_{PS40} from the experimental values of $\phi_m^\infty|_{S_{PS40}}$ (light blue) and $\phi_m^\infty|_{C_{PS40}}$ (orange), respectively: $\mu_r^{\phi_m^\infty}|_{S_{PS40}} = 0.03 \pm 0.02$ and $\mu_r^{\phi_m^\infty}|_{C_{PS40}} = 0.10 \pm 0.01$.

Figure 18 displays the experimental measurements of η_r (coloured symbol) for spherical PS particles (blue discs) and crushed PS particles (orange squares) in aqueous solution $AQ0$, when $\Sigma_{12} \approx 10^{-2}$ Pa (frictionless case: $\Sigma_{12} \ll \sigma_{in}^{fft} \leftrightarrow \mu_s = 0$). As expected, the variation of the reduced viscosity η_r with the volume fraction ϕ follows a Maron–Pierce law (coloured solid straight lines in figure 18, see (3.3)) (Peters *et al.* 2016; Lobry *et al.* 2019). Analogous to § 3.1.2, the fit using (3.3) has been done for $\alpha = 0.85$ and a confidence area is displayed according to the fits of the experimental data when $\alpha = 0.65$ and $\alpha = 1$. The result of the fit of η_s as function of ϕ gives $\phi_m \approx 0.66 \pm 0.01$ for the suspension made of spherical particles (blue solid line) whereas $\phi_m \approx 0.66 \pm 0.02$ for the suspension made of the non-spherical particles (orange dashed line). Several observations can be underlined from this result. First, in the case of frictionless spherical particles, the value of the jamming fraction is in good agreement with the literature (Mari *et al.* 2014; Gallier *et al.* 2018; Singh *et al.* 2018) and this confirms that the suspension is frictionless.

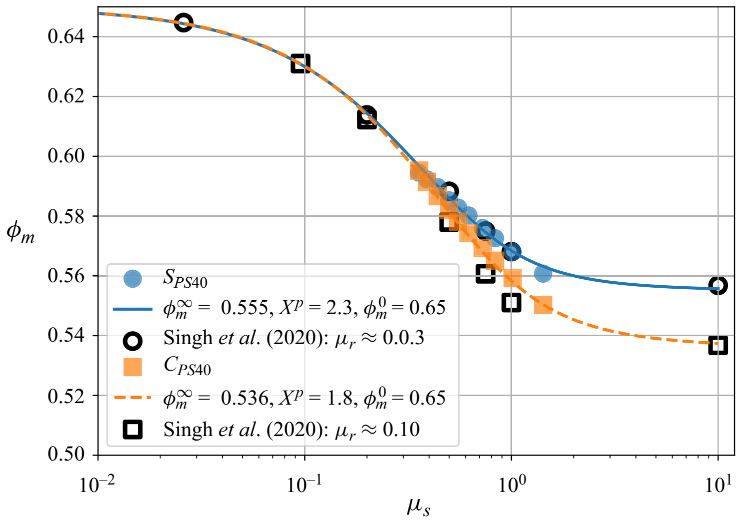

Figure 17. Variation of the jamming volume fraction, ϕ_m, as a function of the sliding friction coefficient, μ_s. The coloured symbols are deduced from the experimental determination of ϕ_m for S_{PS40} (blue circles) and C_{PS40} (orange squares), and μ_s is determined from (3.6) with $\mu_s^\infty = 0.2$, $\Sigma_c = 10$ Pa and $m = 0.5$. The coloured lines are displayed from the variable sliding friction model (see (3.6) and (3.7)) used to fit the experimental data in figure 15 for the suspensions S_{PS40} (blue solid line) and C_{PS40} (orange dashed line). The variation of $\phi_m(\mu_s)$ is compared for each suspension with the numerical results from Singh *et al.* (2020) (open black symbols) for $\mu_r = 3 \times 10^{-2}$ (circles) and $\mu_r = 1 \times 10^{-1}$ (squares).

Second, it confirms our previous choice to have assumed $\phi_m^0 \approx 0.65$ in order to fit the experimental data for $\phi_m(\Sigma_{12})$ of the suspensions C_{PS40} and S_{PS40} by (3.6) and (3.7). Finally, $\phi_m^0 \approx \phi_m|_{\text{crushed PS in AQ0}} \approx \phi_m|_{\text{spheres PS in AQ0}}$ is consistent with the numerical results of Singh *et al.* (2020) who found that ϕ_m is independent of μ_r when $\mu_s \to 0$.

We mention that some literature (Donev *et al.* 2004; Baule & Makse 2014; Kallus 2016) shows that particles having a shape which deviates slightly from spheres are characterised by a *random close packing* concentration, ϕ_m^{RCP}, which is slightly larger than the known value for spheres, $\phi_m^{RCP}|_{spheres} = 0.64$. To the best of the authors' knowledge, there is no strong evidence in the literature showing that the jamming volume fraction ϕ_m^0 (frictionless case: $\mu_s = 0$) and ϕ_m^{RCP} have to be equal, even though it is known that both have the same value in the case of spherical particles. In the present paper, we find that $\phi_m^0|_{\text{crushed PS}} \approx \phi_m^0|_{\text{spheres PS}}$, but it is possible that a slight difference is hidden by the uncertainties. Nevertheless, we want to emphasise that, although the value of ϕ_m^0 in (3.7) plays a significant role in the high-shear-stress regime ($\Sigma_{12} \gtrsim 10^2$ Pa), the shape-induced rolling resistance, related most strongly to ϕ_m^∞ rather than ϕ_m^0, dominates the low-shear-stress regime ($\Sigma_{12} \lesssim 10^1$ Pa).

In the second part of the present paper, we describe how we can determine a value of μ_r for each type of particles (spheres and crushed), based on image analysis. The goal is to compare these new values with the ones predicted by the combination of the numerical works of Singh *et al.* (2020) based on shear rheology measurements coupled with the experimental data $\phi_m(\Sigma_{12})$ (see in §§ 3.2.2 and 3.2.3) that we recall here: $\mu_r^{\phi_m^\infty}|_{S_{PS40}} = 0.03 \pm 0.02$ and $\mu_r^{\phi_m^\infty}|_{C_{PS40}} = 0.10 \pm 0.01$.

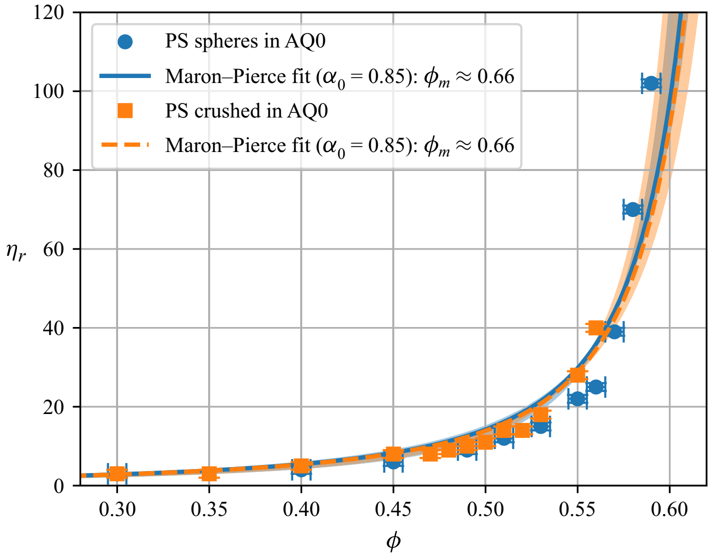

Figure 18. Variation of the shear viscosity, η_r, against volume fraction, ϕ, for two different suspensions: the first made of the same spheres as in S_{PS40} (blue circles) and the second made of the same crushed particles as in C_{PS40} (orange squares). Here, the PS particles are dispersed in an aqueous solution ($\eta_0 = 10^{-3}$ Pa s). The two suspensions sheared at $\Sigma_{12} = 10^{-2}$ Pa in a vane tool geometry are frictionless ($\mu_s = 0$). A fit of the experimental data by (3.3) ($0.65 \leqslant \alpha_0 \leqslant 1$) gives $\phi_m \approx 0.66 \pm 0.01$ for the suspension made of spheres (blue solid line) whereas $\phi_m \approx 0.66 \pm 0.02$ for the suspension made of the non-spherical particles (orange dashed line).

4. Image analysis study

In this section, we focus on the direct determination of the value of the rolling friction coefficient, μ_r, to be compared with the value, $\mu_r^{\phi_m}$, inferred from our rheological measurements and the simulations of Singh *et al.* (2020) (see figure 16). Nevertheless, we note that the treatment of a non-spherical particle by a single rolling friction coefficient on a sphere is an approximation. It would not be exact for two reasons. One is that the resistance to rolling of the non-spherical particle would be different at different parts of the surface. The other is that the static rolling resistance one needs to overcome to initiate rolling could be larger than the time-averaged dynamic rolling resistance one needs to balance to maintain rolling. This difference was minimised by Estrada *et al.* (2011) by considering a uniform polygon. We want to determine how well either of these rolling friction coefficients helps to describe a more irregular but still compact particle rolling resistance.

4.1. *Characterising quantities of particle shape*

To the best of the authors' knowledge, a precise measurement of μ_r between a pair of particles is much more difficult than the measurement of μ_s, which can be done by AFM measurements (Chatté *et al.* 2018; Hsu *et al.* 2018; Arshad *et al.* 2021; Le *et al.* 2023). It is even more difficult for crushed particles with irregular shapes which require even more statistics. It is common in granular media to determine μ_r by letting a particle roll over a slope (Agarwal *et al.* 2021). But the determination of μ_r by this method can be very complicated or nearly impossible for small particles or particles with a large deviation from spherical shape. Because of these experimental limits, we have chosen here to use a novel

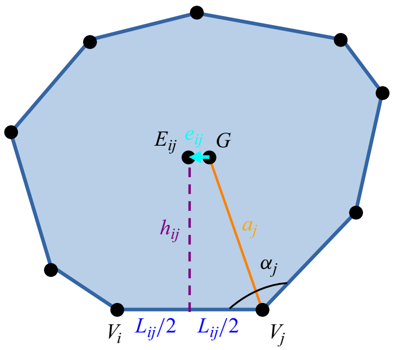

Figure 19. Sketch of a crushed particle (blue area), considered as an irregular convex polygon with a centre of mass G. The sides of the polygon/crushed particle are outlined in a darker blue. The vertices connecting each side are displayed as dark points. Here, L_{ij} is the length of a side connecting two successive vertices, V_i and V_j. The radius a_j is the length of the segment connecting G to the vertex V_j. We use h_{ij} to denote the height of the centroid G above the segment V_iV_j. The black point E_{ij} is on the bisector of the segment V_iV_j and at the same height h_{ij} from the segment V_iV_j as G. The eccentricity of the particle/polygon related to its side V_iV_j is defined as the ratio of the length of the vector $\boldsymbol{e_{ij}}$, denoted $|\boldsymbol{e_{ij}}|$, to the projected diameter, d.

method introduced by Agarwal *et al.* (2021) and Tripathi *et al.* (2021), based on image analysis of static grains to calculate the rolling friction coefficient without considering any material properties of the particle. The basic principle of this novel method is to approximate the projected image of a given particle as a polygon that we can characterise by measuring:

(i) the aspect ratio, a_{ratio}, defined as the ratio of the longest 'height' (i.e. the length between the centre of mass, G, and a side V_iV_j) of the polygon over the smallest one: $a_{ratio} = h_{ij}^{max}/h_{ij}^{min}$;
(ii) the number of sides, n_s;
(iii) the internal angle of each vertex, α_j;
(iv) the length of each side, L_{ij};
(v) the eccentricity associated with each side, $|\boldsymbol{e_{ij}}|/d$.

A qualitative schema of an irregular polygon is displayed in figure 19 to help visualise the different characterising quantities that we aim to measure. Regarding the vector $\boldsymbol{e_{ij}}$, we want to underline that $\boldsymbol{e_{ij}} = \boldsymbol{GE_{ij}}$. As we show later, the parameter e_{ij}, the horizontal component of $\boldsymbol{e_{ij}}$ can be negative or positive depending on the relative positions of E_{ij}, G and V_j. The eccentricity is then defined as the magnitude of $\boldsymbol{e_{ij}}$.

4.1.1. *Approximation of particles projected area as an irregular convex polygon*

Figure 20 shows four examples of 2D approximations as irregular convex polygons for the images of particles composing the suspensions S_{PS40} (a,c) and C_{PS40} (b,d). The basic images are taken with a microscope (examples of basic photos shown in figure 3) with an approximate scale of 80 pixels per particle (projected) diameter. We recall that the projected diameter, d (see figure 5), for a crushed particle corresponds to the diameter of a sphere having the same projected area as the non-spherical particle. Note that, from the start, images with well-separated particles are captured, but if two or more particles are not distinct enough (see figure 3), they are simply not taken into account to compute μ_r. Moreover, we want to emphasise that spherical particles, such as those in figure 20(a,c),

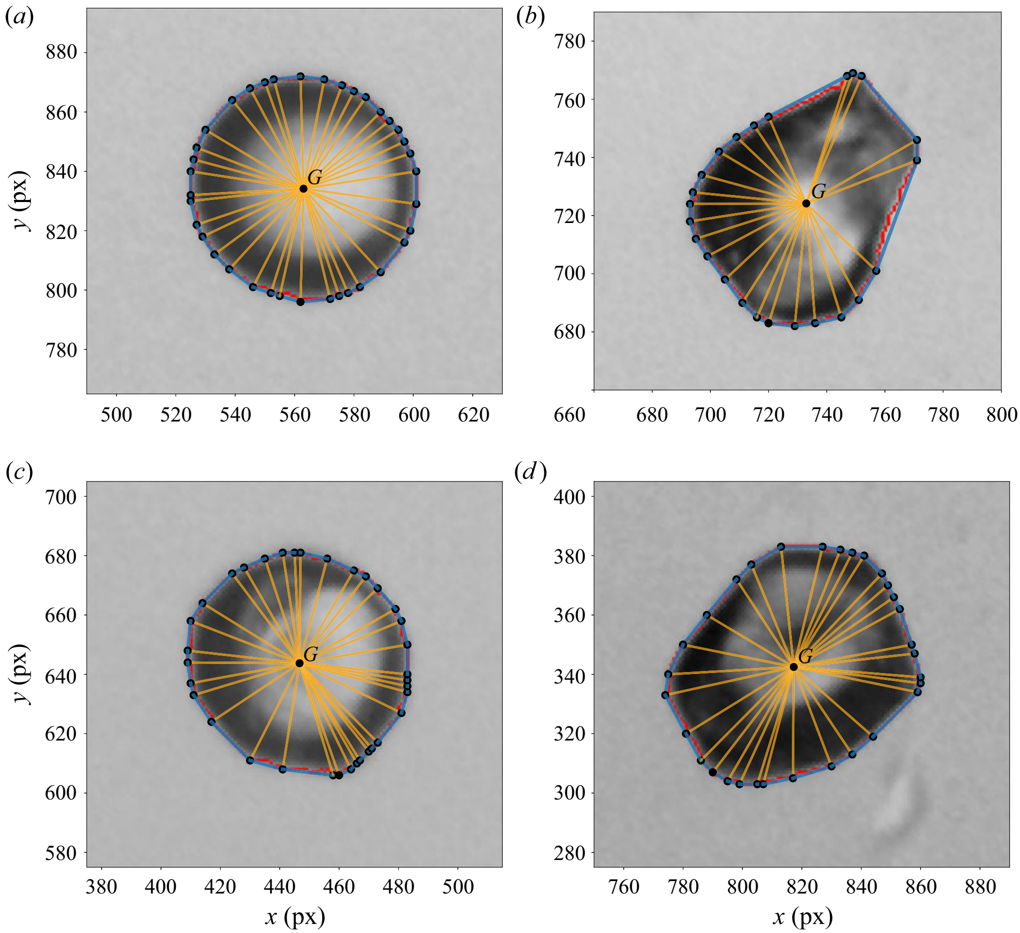

Figure 20. Examples of 2D approximation by an irregular convex polygon for particles composing the suspensions S_{PS40} (*a*,*c*) and C_{PS40} (*b*,*d*). The sides of a polygon are coloured in blue whereas the vertices are marked as black dots. The centre of mass G of the polygon/particle is also located and orange straight lines connecting the centroid G to each vertex are displayed. The red pixels delimit the contour detected by the *segmentation process*. Scale: 'diameter' of particle $\sim$ 80 px.

are also present in C_{PS40}. In the end, the resulting characterising quantities of particles presented above are determined for approximately 600 particles for each type of particle.

The image analysis process is described in Appendix B. The data for the physical particles are compared with results for 10 000 'reference' numerical spheres with similar diameters as the real particles, i.e. in the range $70 \leqslant 2a \leqslant 90$ px. This comparison allows us to examine the effect of the image resolution on the properties of the particles, which in all cases are approximated as polygons.

4.1.2. *Image analysis results on characteristic quantities of particles shape*

Once the coordinates $(V_{i,x}, V_{i,y})$ of each vertex V_i for a given polygon/particle are known, all the characteristic physical quantities for a captured polygon/particle (see schema in figure 19) can be determined. In particular, the area A_p and the location (x_G, y_G) of the centre of mass G of each particle/polygon are determined as follows:

$$A_p = \frac{1}{2}\sum_{i=0}^{n_s-1} \det(Vi, Vj) = \frac{1}{2}\sum_{i=0}^{n_s-1}\left[V_{i,x}V_{j,y} - V_{j,x}V_{i,y}\right], \tag{4.1}$$

$$x_G = \frac{1}{6A_p}\sum_{i=0}^{n_s-1}\left[(V_{x,i} + V_{x,j})\det(V_i, V_j)\right], \tag{4.2}$$

$$y_G = \frac{1}{6A_p}\sum_{i=0}^{n_s-1}\left[(V_{y,i} + V_{y,j})\det(V_i, V_j)\right], \tag{4.3}$$

with $j = i + 1$, except if $i = n_s - 1$, then $j = 0$.

In addition to the size distribution already shown in figure 5 where we observed that crushed and spherical particles have roughly the same size ($d \sim 40\,\mu_m$, with a slight larger degree of polydispersity for the crushed particles), figure 21 displays the distribution of the values of characteristic physical quantities determined for the 'reference' perfectly smooth spheres (in green), the real spherical particles in S_{PS40} (in blue) and the real crushed particles in C_{PS40} (in orange). One can observe that the particles from S_{PS40} (in blue) are mainly spheres since the differences from the reference data (in green) are small as indicated by:

(i) the aspect ratio of the particles in S_{PS40} is close to 1 ($a_{ratio}^{S_{PS40}} \lesssim 1.2$ with 90 % of $a_{ratio}^{S_{PS40}} \lesssim 1.1$);
(ii) the number of segments per polygon and the length of the sides are comparable between the spheres from S_{PS40} and the 'reference' perfectly smooth spheres ($\langle n_s^{S_{PS40}}\rangle \sim \langle n_s^{ref}\rangle \approx 35$ and $\langle L_{ij}/d\rangle^{S_{PS40}} \sim \langle L_{ij}/d\rangle^{ref} \sim 10^{-1}$);
(iii) the angles are nearly the same ($\langle\alpha_j\rangle^{S_{PS40}} \sim \langle\alpha_j\rangle^{ref} \approx 170^\circ$);
(iv) the eccentricity for the beads of S_{PS40} is very small ($(|\boldsymbol{e_{ij}}|/d)^{S_{PS40}} \lesssim 10^{-1}$ including 90 % of $(|\boldsymbol{e_{ij}}|/d)^{S_{PS40}} \lesssim 5.10^{-2}$).

The comparison of the 'reference' spheres and the spherical particles of the suspension S_{PS40} on α_j, L_{ij} and $|\boldsymbol{e_{ij}}|/d$ allows us to characterise the slight deviation from perfect spheres, which is much less than the deviation of crushed particles from spherical shapes.

At first glance, one can observe that the global shape of crushed particles does not deviate much from a sphere. In particular, Figure 21(*a*) shows that $a_{ratio} < 1.5$ for crushed particles, with two-thirds of $a_{ratio}^{C_{PS40}} \lesssim 1.2$. In addition, the crushed particles from C_{PS40} and the spheres from S_{PS40} are both globally approximated as polygons notably having:

(i) the same number of sides since $\langle n_s^{C_{PS40}}\rangle \sim \langle n_s^{S_{PS40}}\rangle \approx 35$;
(ii) the same global angle since $150^\circ \leqslant \alpha_j \leqslant 180^\circ$ for ~88 % of $\alpha_j^{C_{PS40}}$ and ~96 % of $\alpha_j^{S_{PS40}}$;
(iii) the same average length of polygon sides ($\langle(L_{ij}/d)^{C_{PS40}}\rangle \sim \langle(L_{ij}/d)^{S_{PS40}}\rangle \sim 0.1$).

Moreover, the mean normalised eccentricity $\langle(|\boldsymbol{e_{ij}}|/d)^{C_{PS40}}\rangle$ remains globally small. For instance, approximately 60 % of the sides of polygon for crushed particles are characterised by a ratio $(|\boldsymbol{e_{ij}}|/d) \leqslant 5 \times 10^{-2}$ whereas it is 80 % for the spheres of S_{PS40}. Approximately 85 % of the ratios $|\boldsymbol{e_{ij}}|/d$ are less than 10^{-1} for crushed particles, whereas 95 % are less than 10^{-1} for the spheres of S_{PS40}.

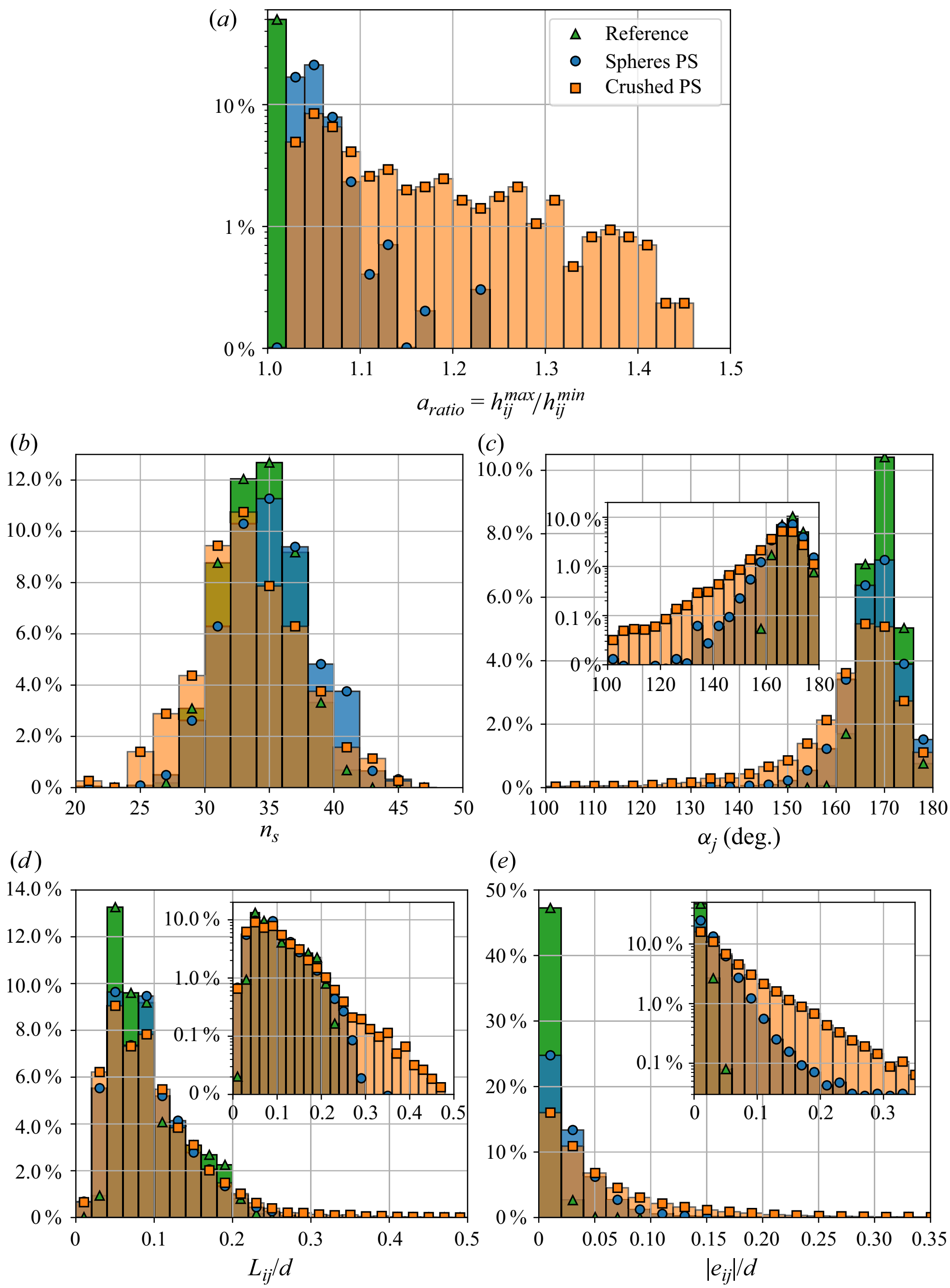

Figure 21. Distribution of the values of (*a*) polygonal aspect ratio $a_{ratio} = h_{ij}^{max}/h_{ij}^{min}$, (*b*) number of segments per particle n_s, (*c*) internal angle α_i at each vertex V_i, (*d*) relative length L_{ij}/d and (*e*) eccentricity $|\boldsymbol{e_{ij}}|/d$ measured across all the particles for the suspensions S_{PS40} (blue) and C_{PS40} (orange). For a_{ratio} and n_s, the statistics include roughly $N \sim 600$ particles for each type of suspension, whereas for α_j, L_{ij}/d and $|\boldsymbol{e_{ij}}|/d$, the computation is done for all the vertices V_i of all the polygons: $\langle n_s \rangle \times N \sim 2 \times 10^4$ data for each suspension. Inset in (*c*,*d*,*e*): Logarithmic *y*-scale is used to highlight the smallest values of α_j and the largest values of L_{ij}/d and $|\boldsymbol{e_{ij}}|/d$, respectively. The data from real suspensions are compared with the results (in green) obtained by doing the same image analysis process on a numerical image of perfectly smooth spheres that we use as a reference.

However, significant differences between the two types of particles are brought out at the same time by figures 21(*a*), 21(*c*) and 21(*e*). On these three specific graphs, we observe as expected that the crushed particles from C_{PS40} are indeed characterised by:

(i) an aspect ratio $a_{ratio} \gtrsim 1.2$ for one-third of the particles;
(ii) a larger portion of 'small' angles than in the case of particles from S_{PS40} ($\sim$15 % of $\alpha_j^{C_{PS40}} \lesssim 155^\circ$ against $\lesssim$4 % of $\alpha_j^{S_{PS40}}$);
(iii) a larger portion of high eccentricity ($\sim$30 % of $(|\boldsymbol{e_{ij}}|/d)^{C_{PS40}} > 6 \times 10^{-2}$ against $\lesssim$10 % of $(|\boldsymbol{e_{ij}}|/d)^{S_{PS40}}$).

To sum up, all these observations show, in fact, that the shapes of crushed particles in C_{PS40} do not deviate globally from a sphere. However, a small but non-negligible number of their sides are very different from spherical arcs, likely at least enough to induce the rheological differences between C_{PS40} and S_{PS40} observed in § 3.1. More precisely, these different measurements conducted to characterise the shape of particles tend to show that the rheological differences between C_{PS40} and S_{PS40}, if related to the particles shape, are mainly due to the three following quantities: a_{ratio}, α_i and $(|\boldsymbol{e_{ij}}|/d)$. We show in the next section how these are all connected to each other and to μ_r.

4.2. *Determination of the rolling friction coefficient*

4.2.1. *Theoretical approach*

Studies of granular media by Wensrich & Katterfeld (2012), Wensrich, Katterfeld & Sugo (2014), Agarwal *et al.* (2021) and Tripathi *et al.* (2021) have shown that an order of magnitude of μ_r for usage in DEM simulations can often be obtained by measuring the ratio of the average contact eccentricity $\langle e\rangle$ to the projected particle diameter d: $\mu_r \approx \langle e\rangle/d$. This ratio is plotted in figure 21(*e*) for the two studied suspensions in the present paper. We have measured $\langle|\boldsymbol{e_{ij}}|/d\rangle^{S_{PS40}} \sim 5 \times 10^{-2}$ and $\langle|\boldsymbol{e_{ij}}|/d\rangle^{C_{PS40}} \sim 10^{-1}$. Interestingly, one can observe that these values are in quite good agreement with the values previously predicted by the combination of the works of Singh *et al.* (2020) and the determination of $\phi_m(\Sigma_{12})$: $\mu_r^{\phi_m^\infty}|_{S_{PS40}} \approx 0.03 \pm 0.02$ and $\mu_r^{\phi_m^\infty}|_{C_{PS40}} \approx 0.10 \pm 0.01$, which confirms the empirical proposition that the eccentricity can be used to estimate μ_r. However, a drawback of this method to calculate μ_r is that it is limited to particles whose shape does not deviate strongly from a sphere. For instance, it cannot be applied to regular polygonal particles (Estrada *et al.* 2011) for which we can expect obviously a higher rolling resistance than spheres despite the fact that their eccentricities are zero. Thus, we will follow and build upon the more fundamental approach of Estrada *et al.* (2011), in which μ_r is derived based on the torque required for rolling which in turn is related to the particle shape parameters.

Figure 22 displays a simple sketch of a crushed particle approximated here as an irregular convex polygon with centre of mass G and number of sides n_s, rolling from the left to the right around one of its vertices (that named V_j on the schematic in figure 22) as a result of a tangential force $\boldsymbol{F_T}$ applied at the centroid G. We consider the conditions such that the irregular convex polygon/particle can only roll ($\mu_s \gg \mu_r$, Estrada *et al.* 2008). As shown in figure 22, a normal force $\boldsymbol{F_N}$ applied at G offers a resistance to the particle's rolling, and rotation occurs if and only if

$$\Gamma_{F_T} > \Gamma_{F_N}, \tag{4.4}$$

where Γ_{F_T} is the torque which tends to make the particle roll, and is defined as $\Gamma_{F_T} = a_j \times \|\boldsymbol{f_T}\|$. Here Γ_{F_N} is the rolling resistance torque and is defined as $\Gamma_{F_N} = a_j \times \|\boldsymbol{f_N}\|$.

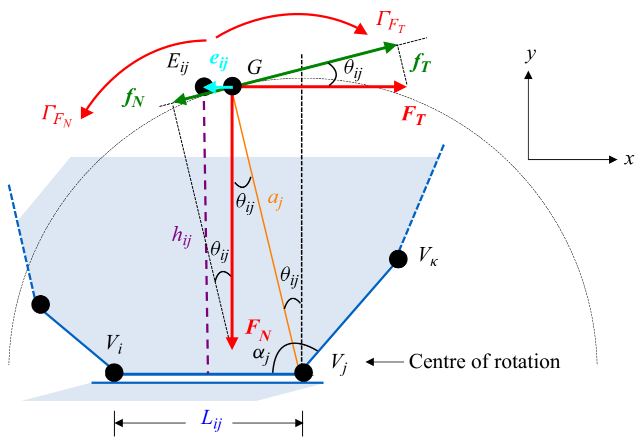

Figure 22. Schema based on the first sketch drawn in figure 19 of a partial crushed particle (blue area), considered as an irregular convex polygon with a centre of mass G. Here, the vertices V_i and V_j are the two vertices considered initially in direct contact with another particle. The forces $\boldsymbol{F_T}$ and $\boldsymbol{F_N}$ are the tangential and normal forces applied at G, respectively. The force $\boldsymbol{f_T}$ is the projection of $\boldsymbol{F_T}$ on the tangent passing by G of the circle of centre V_j and radius a_j. In other words, $\boldsymbol{f_T}$ is the component of $\boldsymbol{F_T}$ that makes the polygon roll from left to right around V_j by applying a torque Γ_{F_T}. Similarly, $\boldsymbol{f_N}$ is the component of $\boldsymbol{F_N}$ that offers a resistance for the polygon to roll around V_j by applying a torque Γ_{F_N}. In this scenario, it is important to understand that the particle motion is from left to right and the particle can only roll (no sliding). In fact, a normal contact force opposing $\boldsymbol{F_N}$ and a sliding friction force opposing $\boldsymbol{F_T}$ are acting at the contact point V_j to prevent it from sliding or moving vertically, but they are not represented here for simplicity. The angle θ_{ij} corresponds to the angle between the vectors $\boldsymbol{GV_j}$ and $\boldsymbol{F_N}$.

The forces $\boldsymbol{f_T}$ and $\boldsymbol{f_N}$ are the parts of the applied forces $\boldsymbol{F_T}$ and $\boldsymbol{F_N}$, respectively, which contribute to the corresponding torques, and are defined as (see figure 22)

$$f_T = F_T \times \cos\theta_{ij} \quad \text{and} \quad f_N = F_N \times \sin\theta_{ij}. \tag{4.5a,b}$$

The angle θ_{ij} corresponds to the angle formed by the vectors $\boldsymbol{GV_j}$ and $\boldsymbol{F_N}$ when the polygon/particle rolls around its vertex V_j from left to right. By coupling (4.4) and (4.5*a*,*b*), we obtain the following condition for the particle to roll around V_j from left to right:

$$F_T > F_N \times \tan\theta_{ij}. \tag{4.6}$$

Obviously, the value of θ_{ij} evolves during the rotation of the particle and, as a result, so does the force required to make the particle roll. Figure 23 displays a qualitative sketch of the horizontal force $\boldsymbol{F_T}$ that must be applied at the centre of mass G as function of the rotation angle φ, in order to make an irregular polygon/crushed particle (composed of five sides) roll over its entire perimeter. One can then observe that the resistance for the particle to roll around one of its vertices is locally maximum at the start of the rotation around the given vertex.

According to the literature (Estrada *et al.* 2008, 2011; Singh *et al.* 2020), the rolling friction law between two grains of radii a_1 and a_2 defines the maximum torque transmitted by the contact from the rolling friction coefficient μ_r as $\Gamma_{roll}^{max} = \mu_r l F_N$, with $l = a_1 + a_2$. By assuming that a given particle rolls around its vertex V_j on a mirror particle in the studied suspensions S_{PS40} and C_{PS40} (consistent with suspensions roughly monodisperse and $a_{ratio} \sim 1$), we have $l = 2a_j$ which then leads to $\Gamma_{roll}^{max}/a_j = 2\mu_r F_N$. Thus, the applied tangential force F_T to roll a sphere equivalent to a crushed particle would have to be greater or equal to Γ_{roll}^{max}/a_j (see figure 2). Thanks to this equation and (4.6), the *static*

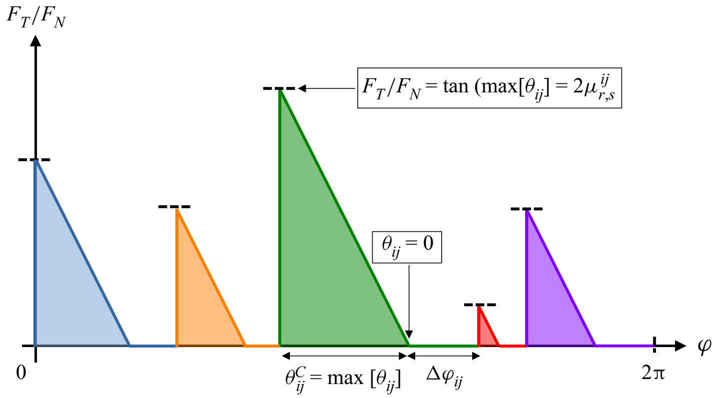

Figure 23. Qualitative sketch of the variation of the ratio F_T/F_N based on (4.6) for an irregular convex polygon with five sides which rolls over its entire perimeter. Each coloured peak labels the rotation of the given pentagon around one of its vertices. Each peak can have a different height because the pentagon is irregular. The height of one peak corresponds to the configuration where the contact with the second particle is 'flat' (for instance, when V_i and V_j are both in contact with a second particle in figure 22), for which $\theta_{ij} = \theta^C_{ij}$. Note that this corresponds to the position where the rolling resistance around the corresponding vertex is maximum. Then, after each coloured peak, $F_T/F_N = 0$ over an angle, $\Delta\varphi$, with $\Delta\varphi_{ij} = \pi - (\alpha_j + \theta^C_{ij})$. This is because $\boldsymbol{F_N}$ no longer induces a rolling resistance once G has been 'vertically' aligned with the vertex/centre of rotation ($\theta_{ij} = 0$). Thus, it is no longer necessary to apply a force $\boldsymbol{F_T}$ to continue rolling around the vertex in the same direction until the next vertex becomes the new contact point/centre of rotation of the particle.

rolling friction coefficient associated with the vertex V_j when the particle rolls in a given direction (here from left to right), denoted $\mu^{ij}_{r,s}$, can be then described as (see figure 22)

$$\mu^{ij}_{r,s} = (1/2)\tan\theta^C_{ij} \quad \text{with } \theta^C_{ij} = \max[\theta_{ij}], \tag{4.7}$$

where θ^C_{ij} is defined as the maximum possible value reached by θ_{ij} when the particle rolls around a vertex V_j in a given direction. As shown in figures 22 and 23, this occurs when the side V_iV_j of the polygon is in contact with the mirror particle. Moreover, we want to point out that, through the parameter θ^C_{ij}, the *static* rolling friction coefficient related to it, $\mu^{ij}_{r,s}$, depends in fact on the length L_{ij} of the segment V_iV_j, the parameter e_{ij} and the height h_{ij} (see figure 22) because

$$\tan\theta^C_{ij} = \frac{(L_{ij}/2) + e_{ij}}{h_{ij}}. \tag{4.8}$$

It is important to note that the value of e_{ij} is directly related to the vector $\boldsymbol{e_{ij}} = \boldsymbol{GE_{ij}}$, and can be positive or negative depending on the relative x position of E_{ij}, G and V_j (see figure 22) and the rolling direction:

(i) if $\boldsymbol{GE_{ij}}$ points in the direction opposite to rolling, then $e_{ij} < 0$;
(ii) if $\boldsymbol{GE_{ij}}$ is the rolling direction, then $e_{ij} > 0$.

Another example which shows the importance of the relative x position of these three points (E_{ij}, G and V_j) is that if G was located to the right of V_j in figure 22 (with the particle rolling from left to right), then $\mu^{ij}_{r,s} = 0$ (as qualitatively shown in figure 23) because the force F_N applied on G no longer induces a resistance torque. We observe that the rolling resistance is larger when:

(i) the length of the side L_{ij} is large; and/or
(ii) e_{ij} increases the value of $(L_{ij}/2) + e_{ij}$; and/or
(iii) the height h_{ij} is small.

These observations from (4.8) are actually quite intuitive. For instance, in the simple case of a regular ($e_{ij} = 0$) 2D polygon with four sides, we can easily imagine that it is harder to roll a cube ($\tan\theta_{ij}^C = 1$) compared with a long rectangle laying on its small side (on the width, $\tan\theta_{ij}^C \to 0$). On the other hand, the long rectangle on its long side will be much harder to roll ($\mu_r^{ij} \gg 1$ when $\theta_{ij}^C \to 90^\circ$).

As observed in figure 23, the irregular shape of 2D polygons/crushed particles implies that the *static* rolling friction coefficient $\mu_{r,s}$ associated with a given irregular convex polygon/crushed particle is inhomogeneous in angular space. We have therefore chosen to define $\mu_{r,s}$ of a given particle as equal to the maximum value of $\mu_{r,s}^{ij}$,

$$\mu_{r,s} = \max\left[\mu_{r,s}^{ij}\right] \quad \forall\,(i,j) \in [0, n_s - 1], \tag{4.9}$$

with:

(i) if $i < n_s - 1$, then $j = (i + 1)$;
(ii) if $i = n_s - 1$, then $j = 0$.

The idea behind this choice follows the argument made by Estrada *et al.* (2008). We consider an irregular polygon laid on its side V_iV_j on a plane inclined with an angle θ_{ij}. In order to make the polygon roll down the inclined plane (i.e. to change its side in contact with the inclined plane), the angle of the slope must be larger than a critical value: $\theta_{ij} \gtrsim \theta_{ij}^C$. By rolling (without inertia), if the new critical angle θ_{jk}^C (associated with the new side V_jV_k in contact with the plane) is lower than the previous one (i.e. θ_{ij}^C), then rolling continues. However, if a subsequent segment of the polygon has a higher value of critical angle, the polygon stops rolling. In determining $\mu_{r,s}$, we also consider the maximum resistance between the two possible directions of rotation.

Thus, the *static* rolling resistance is related to the torque required to initiate rolling (assuming the particle stopped rolling at its most resistant angle). However, it is important to understand that another rolling resistance can be related to the work required to maintain rolling at a constant angular velocity. Both should be important in different parts of a sheared suspension (and at different times at the same location). Analogous to Estrada *et al.* (2011), this second rolling resistance can be determined by calculating the total work required to roll a non-spherical particle over its entire perimeter, P_p, and then balancing it with the total work of an equivalent sphere (of the same perimeter P_p as the first one) with a resistance for rolling motion (i.e. a work balance instead of a torque balance). The resistance to rolling motion induced by the particle shape would be then characterised by a *dynamic* friction coefficient, $\mu_{r,d}$, instead of the *static* one, $\mu_{r,s}$. In figure 23, it would be then determined from the total (coloured) area under the curve F_T/F_N, instead of the maximum peak, and one can expect that $\mu_{r,d} \leqslant \mu_{r,s}$. We describe the method of calculating $\mu_{r,d}$ analogous to Estrada *et al.* (2011) in Appendix C, finally defined as

$$\mu_{r,d} = \frac{1}{2P_p}\sum_{j=0}^{n_s-1} \delta y_j', \tag{4.10}$$

with:

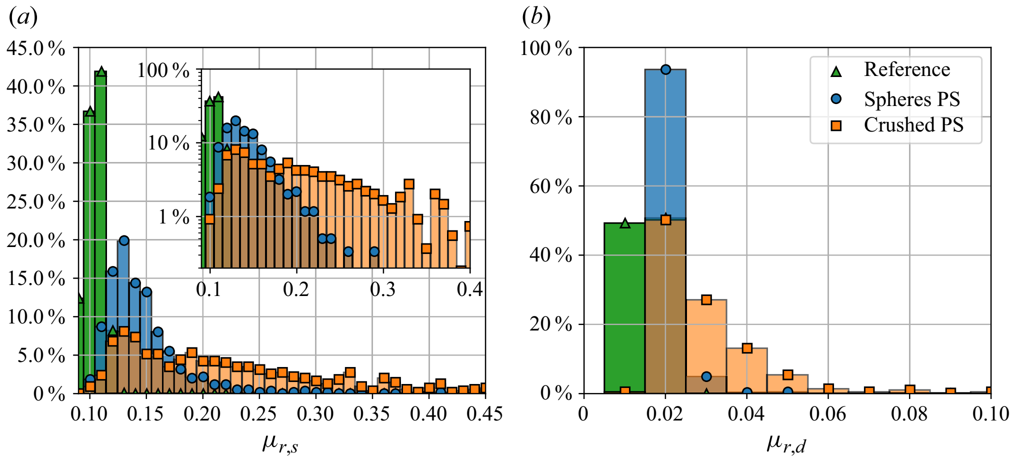

Figure 24. Distribution of (*a*) the static rolling friction coefficient, μ_r and (*b*) the dynamic rolling friction coefficient, $\mu_{r,d}$, both determined by image analysis for the reference perfectly smooth spheres (in green), the spherical particles composing S_{PS40} (in blue) and the crushed particles from C_{PS40} (in orange).

(i) $\delta y_j' = a_j - h_{ij}$ if $a_i < \sqrt{L_{ij}^2 + h_{ij}^2}$;
(ii) else $\delta y_j' = 0$.

In fact, one can note that $\mu_{r,d}$ is related directly to the averaged particle dilatancy, which is in agreement with the work of Estrada *et al.* (2011).

4.2.2. *Image analysis results for the rolling friction coefficient*

Figure 24 displays the measured distribution of (*a*) the maximum *static* rolling friction coefficient $\mu_{r,s}$ and (*b*) the *dynamic* friction coefficient $\mu_{r,d}$, based on (4.9) and (4.10), respectively. Before discussing these graphs, we emphasise that our geometrical approach to determine the coefficients $\mu_{r,s}$ and $\mu_{r,d}$ is correct and independent of the method of measurements or resolution. We point out that the measurements on the 'reference' perfectly smooth spheres (in green in figure 24) give a maximum resolution (i.e. lower limit for the values) on the order of 10^{-1} for $\mu_{r,s}$ and 10^{-2} for $\mu_{r,d}$. These limits for $\mu_{r,s}$ and $\mu_{r,d}$ are induced by the discretisation process which divides a particle contour into a finite number of segments and could be reduced by increasing the resolution of the images. Nevertheless, the resolution is estimated to be sufficient here because the magnitudes of the experimental data appear to be higher than these limits. Moreover, it is expected that the value of $\mu_{r,s}$ should not be affected at all by the resolution limit because it takes into account the maximum rolling resistance, unlikely induced by a spherical part of the particle. It is true that the resolution limit might play a role in the determination of the value of the *dynamic* rolling friction coefficient: the values of $\mu_{r,d}$ are likely overestimated because the rolling resistance related to the spherical part of a particle would tend to decrease the value of $\mu_{r,d}$. This is the reason why the relative uncertainties on $\mu_{r,d}$ are quite large. Moreover, as we show later, the value of $\mu_{r,d}$ is already lower than the value of the rolling friction coefficient determined previously from ϕ_m^∞.

Figure 24(*a*) displays the measured distribution of the *static* rolling friction coefficient, $\mu_{r,s}$. We observe that the values of $\mu_{r,s}$ associated with the crushed particles (in orange) are globally larger and more broadly distributed than those associated with the spheres from S_{PS40} (in blue). This result is quite intuitive because, for a given particle, we consider only the maximum value of $\mu_{r,s}^{ij}$ to determine $\mu_{r,s}$. As it is unlikely that the spherical part of a crushed particle is taken into account following this, the difference from spheres is then emphasised. One can even note that the values of $\mu_{r,s}^{S_{PS40}}$ slightly differ from those determined for perfectly smooth spheres (in green in figure 24), which could come from real deformations of spheres composing S_{PS40}. The averaged value of $\mu_{r,s}$ for each suspension is measured to be $\overline{\mu_{r,s}}|_{S_{PS40}} \approx 0.13$ and $\overline{\mu_{r,s}}|_{C_{PS40}} \approx 0.2$. Thus, on the one hand, we have $\mu_{r,s}^{S_{PS40}} < \mu_{r,s}^{C_{PS40}}$. On the other hand, it is actually quite satisfactory that $\mu_r^{\phi_m^\infty} \lesssim \mu_{r,s}$ for the two studied suspensions (recall that we determined $\mu_r^{\phi_m^\infty}|_{S_{PS40}} \approx 0.03 \pm 0.02$ and $\mu_r^{\phi_m^\infty}|_{C_{PS40}} \approx 0.10 \pm 0.01$), because the *static* rolling friction coefficient, $\mu_{r,s}$, should characterise the maximum rolling resistance.

Figure 24(*b*) displays the measured distribution of the *dynamic* rolling friction coefficient, $\mu_{r,d}$, associated with the crushed particles of C_{PS40} (in orange) and the spheres of S_{PS40} (in blue). As expected, the values of $\mu_{r,d}$ are smaller than the values of $\mu_{r,s}$ for each studied suspension, and we still observe that $\mu_{r,d}^{S_{PS40}}$ is globally smaller and less distributed than $\mu_{r,d}^{C_{PS40}}$. We found the following averaged values: $\overline{\mu_{r,d}}|_{S_{PS40}} \approx 0.02$ and $\overline{\mu_{r,d}}|_{C_{PS40}} \approx 0.03$. Here, one can note that $\mu_{r,d} \lesssim \mu_r^{\phi_m^\infty}$ for each studied suspension.

Finally, the results of this study show that the globular/crushed PS particle geometry itself is enough to induce the rheological differences observed between C_{PS40} and S_{PS40}. To go further, it is quite satisfactory that $\mu_{r,d} \lesssim \mu_r^{\phi_m^\infty} \lesssim \mu_{r,s}$ for the two studied suspensions. We think that the experimental method described in the present paper to characterise the resistance to rolling motion induced by particle shape can be considered as another step to estimate the rolling friction coefficient for usage in DEM simulations, because it gives a framework for the value of μ_r for real suspensions made of non-spherical particles. We recall that, in agreement with the works of Agarwal *et al.* (2021) and Tripathi *et al.* (2021) in dry granular media, a more accurate estimation can be obtained by considering the particle eccentricity defined by e/d. However, two limits of this ratio exist: it cannot be considered for particles with a regular polygon shape ($e = 0$) or a shape that deviates too much from a sphere. Therefore, the novelty of the present work is then to give a way of estimating a framework of μ_r, particularly its upper (*static*) and lower (*dynamic*) bounds.

5. Concluding remarks

In this paper, two different but similar monodisperse suspensions have been sheared in a parallel plate rheometer in order to study their rheological behaviours and characterise their differences. More precisely, the main goal of the present paper was to study the influence of particle shape on the rheology of non-Brownian viscous frictional suspensions. Indeed, the rheology of suspensions composed of spherical particles has been studied extensively in the literature. However, understanding of the rheological behaviour of more complex suspensions composed of particles with irregular shape, which are more common in nature, remains more elusive. We have made two different suspensions composed of the same solid PS particles, separately dispersed in the same suspending Newtonian liquid. The only difference between the two lies in the shape of the particles present in each suspension: spheres in the first and crushed PS particles in the second.

We have then characterised the rheological behaviour of these different types of suspension by studying the variation of the jamming volume fraction with shear stress. Our main result shows that the suspension made of crushed particle is more viscous than the suspension made of spheres at small shear stress whereas the viscosity of the two suspensions becomes equivalent at large shear stress. This results in a stronger shear-thinning behaviour for the suspension made of crushed particles. This observation is notably reflected by a jamming volume fraction smaller at low shear stress for crushed particles whereas it is of the same order of magnitude as that for spheres when shear stress increases.

To go further, we have tried to understand the physical mechanism behind this observation, obviously induced by the different particle shapes. The literature pointed out the influence of rolling resistance but two different origins could be related to it and have been proposed: changes of adhesive force strength with particles' local curvature and rolling resistance induced by locally normal contact forces acting at a non-spherical particle surface.

We have proposed two arguments which tend to demonstrate that adhesion is not important for the present rheological measurements. The first has been to show that the applied shear stress in the present study is much larger than the yield stress of suspensions (spheres and crushed). The second (and main) argument has been based on conducting shear reversal experiments and measuring the minimum value of viscosity, η_{min}, and characteristic strains. The measurements of the same η_{min} in the two types of suspensions and characteristic strains typical for non-adhesive particles was in contradiction with what could be expected if adhesive forces had played a significant role.

The second explanation relates the shear-thinning behaviour of both suspensions to a variable sliding friction, μ_s, whereas the larger viscosity at low shear stress for the non-spherical particles is assumed to be related to the particle shape. This physical origin for the shear-thinning behaviour is notably supported in the case of the PS spherical particles by the literature with the works of Lobry *et al.* (2019) coupled with the AFM measurements on the same type of particles done by Arshad *et al.* (2021) and Le *et al.* (2023). Regarding the crushed particles, we have assumed a variation of μ_s with Σ_{12} identical to the spherical particles, based on the fact that the crushed particles and the spherical particles are from the same material and of the same size. Moreover, the global aspect of the crushed particles does not deviate much from spheres. AFM measurements performed on the crushed particles could validate this assumption in the future.

The recent numerical work of Singh *et al.* (2020) has shown that the rolling resistance of solid particles plays a predominant role determining the jamming volume fraction, ϕ_m, when the sliding friction coefficient is large ($\mu_s \gtrsim 0.5$), but has almost no effect when μ_s is small. A quick comparison on the suspensions made of PS spheres and crushed particles in the frictionless case (PS particles in an aqueous solution) has shown no rheological differences, which is consistent with the absence of impact of μ_r when $\mu_s \rightarrow 0$. We have shown that it is possible to fit the variation of the jamming volume fraction with shear stress for both types of suspensions by the same variable sliding friction model (Lobry *et al.* 2019), simply by predicting a smaller value of the jamming volume fraction for crushed particles when the shear stress tends to zero (i.e. sliding friction coefficient grows 'infinite'). The obtained value of ϕ_m^∞ (for which the predominant relative motion is rolling) from the fit (Lobry *et al.* 2019) coupled with the simulations of Singh *et al.* (2020) allowed us to obtain values of the apparent rolling friction coefficient for both types of suspension: $\mu_r^{\phi_m^\infty} = 0.03 \pm 0.02$ and $\mu_r^{\phi_m^\infty} = 0.10 \pm 0.01$ for spheres and crushed particles, respectively.

The last part of the present paper has been focused on an experimental estimation of the rolling friction coefficient for both types of particles studied in the present paper. Faced with the difficulty of performing a direct experimental measurement for such small non-spherical particles, we decided to use an image analysis process consisting of approximating particles as irregular convex 2D polygons to measure the characterising shape parameters such as aspect ratio, internal angle and eccentricity, and finally calculate the values of the *static* rolling friction coefficient associated with each side of each polygon, μ_r^{ij}. The *static* rolling friction coefficient of each particle, $\mu_{r,s}$, has then been defined as the maximum value of all $\mu_{r,s}^{ij}$ characterising each particle. On the other hand, we have also determined the value of the *dynamic* friction coefficient, $\mu_{r,d}$, from the work needed to roll the particle over a distance equal to its own perimeter, analogous to Estrada *et al.* (2011). Therefore, $\mu_{r,d}$ can be then seen as an averaged value to characterise the shape-induced resistance of a particle to rolling motion based on the whole particle shape. In addition to the fact that the particle geometry of the two studied suspensions is enough to explain the rheological differences between the two, we have notably shown that the calculation of these two coefficient values ($\mu_{r,s}$ and $\mu_{r,d}$) gives a framework to estimate the value of μ_r for usage in numerical simulations.

Interestingly, a very good agreement with the recent works of Agarwal *et al.* (2021) and Tripathi *et al.* (2021) has been found and we confirmed that the eccentricity, defined as the ratio e/d, gives a very good estimation of the value of rolling resistance for usage in DEM simulations, as long as the particle shape does not deviate too much from a sphere, and that $e \neq 0$.

To go further, the next step would be to find a way to directly measure the rolling friction coefficient of the particles (as is done by AFM measurements for μ_s), instead of deducing it by an image analysis process. Other difficulties encountered here concern the irregular shape of crushed particles, and the diversity of irregular shapes, which might invalidate the 2D approximation invoked here and make it harder to characterise the rolling resistance for irregular crushed particles. It is also true that different types of solid contact between the particles can exist in the crushed particles. In this paper, we have only considered a scenario where a particle rolls over a 'mirror' particle, but the physics is probably much more complex and it could be interesting to numerically study the distribution of the types of contact in such a suspension. Being aware of this, we think it could be interesting to compare the numerical results of Singh *et al.* (2020) with more regularly defined shapes such as cubic particles or other regular polygonal particles (for which $e = 0$). Small hard fibres ($a_{ratio} \lesssim 2$) could also be an interesting shape. One can note that the angularity explored through the crushed particles in the present study remains close to spheres ($\alpha_j \rightarrow 180^\circ$). Studying cubes or rectangular shapes may then be interesting to explore smaller internal angles domains ($\alpha_j \rightarrow 90^\circ$). It would have the second advantage of increasing the value of μ_r. Indeed, Singh *et al.* (2020) have shown that the influence of μ_r on ϕ_m is very large when $3 \times 10^{-2} \leqslant \mu_r \leqslant 3$. Cubes present this dual advantage of having a well-defined shape and an expected higher friction coefficient: μ_r is expected to be between 0.1 (*dynamic*) and 0.5 (*static*), for which Singh *et al.* (2020) have predicted a much lower jamming fraction, $0.44 \lesssim \phi_m^\infty \lesssim 0.53$. Thus, determining ϕ_m^∞ would show whether static or dynamic is more important. A rectangular shape ($a_{ratio} \lesssim 2$) offers two very different side lengths and allows one to study further the influence of the angular dependency of μ_r.

Acknowledgements. We thank Y. Al-Majali and Y. Madraki for their assistance with crushing the particles, and we thank F. Peters and A. Singh for fruitful discussions. We acknowledge A. Singh for sharing his data from Singh *et al.* (2020).

Funding. This work was supported by the National Science Foundation (NSF; grant numbers CBET-1554044-CAREER and CBET-2210322).

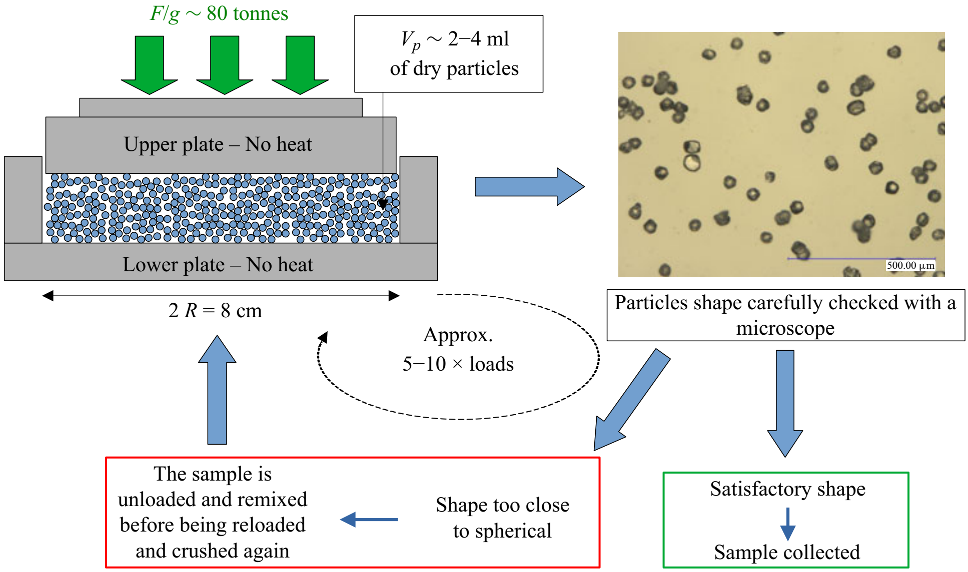

Figure 25. Sketch of the compression process used to mold the PS particles shape: very long, tedious and meticulous work done by Yahya Al-Majali and Yasaman Madraki in order to get a few particles.

Declaration of interests. The authors report no conflict of interest.

Author ORCIDs.
Enzo d'Ambrosio https://orcid.org/0000-0002-4499-3580;
Donald L. Koch https://orcid.org/0000-0002-5474-879X;
Sarah Hormozi https://orcid.org/0000-0001-5712-1178.

Appendix A. Process to crush the PS particles

Compression molding by a series of successive loading phases were done in order to crush the spherical PS particles. Figure 25 provides the schematics of the process. A dry sample of roughly 2–4 ml of PS beads were put between 2 steel plates, forming a layer about 10 particles thick and then compressed at room temperature by a load equivalent to approximately 80×10^3 kg (80 tonnes) for roughly 10 min. The particles were then observed under a microscope in order to check their shape. The process was then repeated if the shape of the particles was not satisfactory. Eventually, the loading operation on a given sample was repeated between 5 and 10 times. The particles were finally sieved to decrease the size distribution. Note that different processes of crushing were tried in order to get the non-spherical particles, notably by either increasing or decreasing the temperature or/and the load force. The process was tedious and very long but was determined to be the most appropriate in order to get the roughly 200 mg desired particle shape at the end.

Appendix B. The image analysis process

The image processing is performed as follows. Each image taken with a microscope is binarised with a local threshold whose value $T(x, y)$ is calculated individually for each pixel (x, y). Here, $T(x, y)$ is a weighted sum (cross-correlation with a Gaussian window) of a 501×501 px^2 neighbourhood of the pixel (x, y) (see the OpenCV cv2.adaptiveThreshold website: https://docs.opencv.org/2.4/index.html). A rough delimitation of each particle in the picture is thus detected. However, the pixels belonging to the interior of a particle, whose grey level can be similar to the background, can be incorrectly identified as not being part of the particle. As a result, the interior of particles is 'filled' (see OpenCV cv2.floodFill) in order to correct it. The projected particles and their well-defined contours (red pixels in figure 20) are then detected through a watershed segmentation process (Vincent & Soille 1991, see OpenCV cv2.watershed). Finally, the contour of each particle is approximated as an irregular convex envelope (see OpenCV cv2.approxPolyDP, coloured in blue in figure 20) for which the (x, y) coordinates of each vertex V_i (black dot except G in figure 20) are known ($0 \leqslant i \leqslant n_s - 1$, with n_s the number of sides of the polygon).

Appendix C. Theoretical approach to determine the dynamic rolling friction coefficient

Let us consider that the centre of mass G travels left to right over a horizontal distance which is given by $\boldsymbol{x_G} = \delta x' + \delta x''$ (see figure 26). Under these conditions, the work required to displace the crushed particle over this given distance can be calculated as

$$W'_p|_j = \boldsymbol{F_N} \cdot \boldsymbol{y_G} = F_N \times \delta y'_j, \tag{C1}$$

where $\boldsymbol{y_G}$ is the vertical vector displacement of the centroid G for which the force F_N exerts a rolling resistance, and its norm is equal to $\delta y' = a_j - h_{ij}$. On the other hand, the work needed to displace a disc, characterised by a dynamic rolling friction coefficient $\mu_{r,d}$, over a distance equal to $\boldsymbol{x_G}$ is

$$W_d = \boldsymbol{F_T} \cdot \boldsymbol{x_G} = 2\mu_{r,d} F_N \times \left(\delta x'_j + \delta x''_j\right). \tag{C2}$$

Assuming equal work, $W'_p|_j = W_d$, we arrive at the following mapping for the *dynamic* friction coefficient associated with the rotation from left to right around V_j:

$$\mu'_{r,d}|_j = \frac{1}{2}\left[\frac{\delta y'_j}{\delta x'_j + \delta x''_j}\right], \tag{C3}$$

where $\delta y'_j = a_j - h_{ij}$, $\delta x'_j = L_{ij}/2 + e_{ij}$ and $\delta x''_j = L_{jk}/2 + e_{jk}$ (with e_{ij} and e_{jk} positive or negative). Note that, in the case for which the particle rolls around V_j from the right to the left, $\mu_{r,d}$ is defined as

$$\mu''_{r,d}|_j = \frac{1}{2}\left[\frac{\delta y''_j}{\delta x'_j + \delta x''_j}\right], \tag{C4}$$

where $\delta y''_j = a_j - h_{jk}$. Obviously, if the polygon is regular ($L_{ij} = L_{jk}$, $e_{ij} = e_{jk} = 0$, $h_{ij} = h_{jk}$), then $\mu_{r,d} = \mu'_{r,d}|_j = \mu''_{r,d}|_j$ and we arrive at the following mapping between $\mu_{r,d}$ and the dilatancy angle ($\psi = \psi'_j = \psi''_j \; \forall j \in [0 \, n_s - 1]$), already found by Estrada *et al.* (2011):

$$\mu_{r,d} = (1/4) \tan\psi \quad \text{with } \psi = \frac{\pi}{2n_s}. \tag{C5}$$

In our case, the polygons are irregular and, thus, the required work to roll around one vertex is not the same for all the vertices of a particle, as is shown qualitatively in figure 23 (the volume of each coloured peak is different). Unlike the *static* friction coefficient, $\mu_{r,s}$, for which we have considered the maximum resistant torque to rolling motion, we define

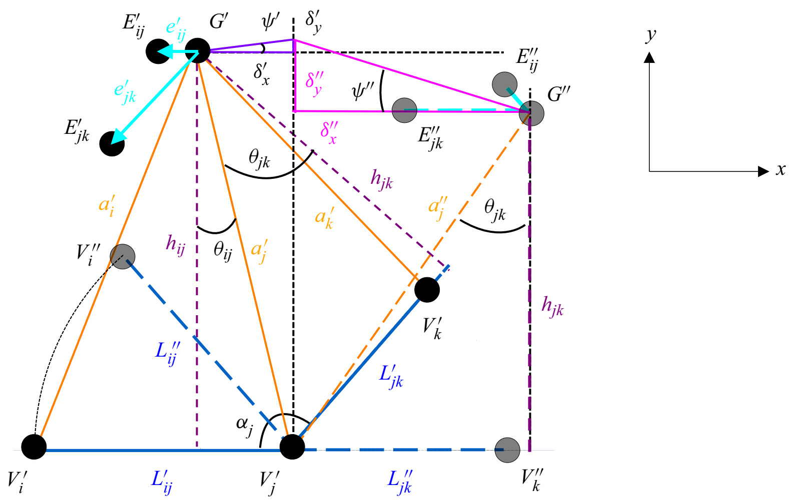

Figure 26. Sketch analogous to figure 22 of a partial crushed particle, considered as an irregular convex polygon with a centre of mass G. Two sides of the polygon/crushed particle, V_iV_j and V_jV_k, are outlined in dark blue. Tangential and normal forces, $\boldsymbol{F_T}$ and $\boldsymbol{F_N}$ (not represented here to avoid overloading the schema), respectively, are applied on the centre of mass G of the particle as shown in figure 22 to create a rolling motion from left to right around V_j. Under these conditions, V_i is the other vertex (with V_j) considered initially in direct contact with the mirrored particle, whereas V_k is that which will be in contact at the end of the rotation around V_j. The initial (prime) location of each point is displayed with a black point and annotated ($'$), whereas the final (second) position is displayed with a transparent dot and annotated ($''$). Analogous to figure 22, α_j corresponds to the internal angle of the polygon/particle at V_j ($\alpha_j = \widehat{V_iV_JV_k}$), θ_{ij} and θ_{jk} are the angles between the segments h_{ij} and GV_j, and h_{jk} and GV_j, respectively. Here h_{ij} and h_{jk} are the heights of G from the segment V_iV_j and V_jV_k, respectively. The eccentricity for the sides V_iV_j and V_jV_k corresponds to the lengths $|\boldsymbol{e_{ij}}|/d$ and $|\boldsymbol{e_{jk}}|/d$, respectively. The angle ψ' (respectively, ψ'') is the dilatancy angle when the particle rolls from the left to the right (respectively, from the right to the left) around V_j.

$\mu_{r,d}$ by considering the whole particle. The sum of the work for rolling over all vertices $W'_p|_j$ (or $W''_p|_j$) corresponds to the total work needed to displace a given particle over a distance equal to its perimeter P_p, and the value of the *dynamic* friction coefficient $\mu_{r,d}$ associated with the given particle can then be determined by the equation

$$\mu_{r,d} = \sum_{j=0}^{n_s-1} \mu'_{r,d}|_j = \frac{1}{2P_p} \sum_{j=0}^{n_s-1} \delta y'_j, \tag{C6}$$

where:

(i) $\delta y'_j = a_j - h_{ij}$ if $a_i < \sqrt{L_{ij}^2 + h_{ij}^2}$;
(ii) else $\delta y'_j = 0$.

References

Acrivos, A., Fan, X. & Mauri, R. 1994 On the measurement of the relative viscosity of suspensions. *J. Rheol.* **38** (5), 1285–1296.

Acrivos, A., Mauri, R. & Fan, X. 1993 Shear-induced resuspension in a Couette device. *Intl J. Multiphase Flow* **19** (5), 797–802.

Agarwal, A., Tripathi, A., Tripathi, A., Kumar, V., Chakrabarty, A. & Nag, S. 2021 Rolling friction measurement of slightly non-spherical particles using direct experiments and image analysis. *Granul. Matt.* **23** (3), 1–14.

ARSHAD, M., MAALI, A., CLAUDET, C., LOBRY, L., PETERS, F. & LEMAIRE, E. 2021 An experimental study on the role of inter-particle friction in the shear-thinning behavior of non-Brownian suspensions. *Soft Matt.* **17** (25), 6088–6097.

BARNES, H.A. 1989 Shear-thickening ("dilatancy") in suspensions of nonaggregating solid particles dispersed in Newtonian liquids. *J. Rheol.* **33** (2), 329–366.

BAULE, A. & MAKSE, H.A. 2014 Fundamental challenges in packing problems: from spherical to non-spherical particles. *Soft Matt.* **10** (25), 4423–4429.

BENDER, J. & WAGNER, N.J. 1996 Reversible shear thickening in monodisperse and bidisperse colloidal dispersions. *J. Rheol.* **40** (5), 899–916.

BLANC, F., D'AMBROSIO, E., LOBRY, L., PETERS, F. & LEMAIRE, E. 2018 Universal scaling law in frictional non-Brownian suspensions. *Phys. Rev. Fluids* **3** (11), 114303.

BLANC, F., LEMAIRE, E., MEUNIER, A. & PETERS, F. 2013 Microstructure in sheared non-Brownian concentrated suspensions. *J. Rheol.* **57** (1), 273–292.

BLANC, F., PETERS, F. & LEMAIRE, E. 2011*a* Experimental signature of the pair trajectories of rough spheres in the shear-induced microstructure in noncolloidal suspensions. *Phys. Rev. Lett.* **107** (20), 208302.

BLANC, F., PETERS, F. & LEMAIRE, E. 2011*b* Local transient rheological behavior of concentrated suspensions. *J. Rheol.* **55** (4), 835–854.

BOYER, F., GUAZZELLI, É. & POULIQUEN, O. 2011 Unifying suspension and granular rheology. *Phys. Rev. Lett.* **107** (18), 188301.

BRIZMER, V., KLIGERMAN, Y. & ETSION, I. 2007 Elastic–plastic spherical contact under combined normal and tangential loading in full stick. *Tribol. Lett.* **25** (1), 61–70.

BROWN, E., FORMAN, N.A., ORELLANA, C.S., ZHANG, H., MAYNOR, B.W., BETTS, D.E., DESIMONE, J.M. & JAEGER, H.M. 2010 Generality of shear thickening in dense suspensions. *Nat. Mater.* **9** (3), 220–224.

BROWN, E. & JAEGER, H.M. 2012 The role of dilation and confining stresses in shear thickening of dense suspensions. *J. Rheol.* **56** (4), 875–923.

BROWN, E. & JAEGER, H.M. 2014 Shear thickening in concentrated suspensions: phenomenology, mechanisms and relations to jamming. *Rep. Prog. Phys.* **77** (4), 046602.

CHATTÉ, G., COMTET, J., NIGUÈS, A., BOCQUET, L., SIRIA, A., DUCOURET, G., LEQUEUX, F., LENOIR, N., OVARLEZ, G. & COLIN, A. 2018 Shear thinning in non-Brownian suspensions. *Soft Matt.* **14** (6), 879–893.

CHOW, A.W., SINTON, S.W., IWAMIYA, J.H. & STEPHENS, T.S. 1994 Shear-induced particle migration in Couette and parallel-plate viscometers: NMR imaging and stress measurements. *Phys. Fluids* **6** (8), 2561–2576.

COMTET, J., CHATTÉ, G., NIGUÈS, A., BOCQUET, L., SIRIA, A. & COLIN, A. 2017 Pairwise frictional profile between particles determines discontinuous shear thickening transition in non-colloidal suspensions. *Nat. Commun.* **8** (1), 1–7.

COUSSOT, P. & PIAU, J.M. 1994 On the behavior of fine mud suspensions. *Rheol. Acta* **33** (3), 175–184.

DAGOIS-BOHY, S., HORMOZI, S., GUAZZELLI, E. & POULIQUEN, O. 2015 Rheology of dense suspensions of non-colloidal spheres in yield-stress fluids. *J. Fluid Mech.* **776**, R2.

D'AMBROSIO, E., BLANC, F. & LEMAIRE, E. 2021 Viscous resuspension of non-Brownian particles: determination of the concentration profiles and particle normal stresses. *J. Fluid Mech.* **911**, A22.

DBOUK, T., LOBRY, L. & LEMAIRE, E. 2013 Normal stresses in concentrated non-Brownian suspensions. *J. Fluid Mech.* **715**, 239.

DONEV, A., CISSE, I., SACHS, D., VARIANO, E.A., STILLINGER, F.H., CONNELLY, R., TORQUATO, S. & CHAIKIN, P.M. 2004 Improving the density of jammed disordered packings using ellipsoids. *Science* **303** (5660), 990–993.

ESTRADA, N., AZÉMA, E., RADJAI, F. & TABOADA, A. 2011 Identification of rolling resistance as a shape parameter in sheared granular media. *Phys. Rev.* E **84** (1), 011306.

ESTRADA, N., TABOADA, A. & RADJAI, F. 2008 Shear strength and force transmission in granular media with rolling resistance. *Phys. Rev.* E **78** (2), 021301.

FALL, A., LEMAITRE, A., BERTRAND, F., BONN, D. & OVARLEZ, G. 2010 Shear thickening and migration in granular suspensions. *Phys. Rev. Lett.* **105** (26), 268303.

FERNANDEZ, N., MANI, R., RINALDI, D., KADAU, D., MOSQUET, M., LOMBOIS-BURGER, H., CAYER-BARRIOZ, J., HERRMANN, H.J., SPENCER, N.D. & ISA, L. 2013 Microscopic mechanism for shear thickening of non-Brownian suspensions. *Phys. Rev. Lett.* **111** (10), 108301.

FRITH, W.J., D'HAENE, P., BUSCALL, R. & MEWIS, J. 1996 Shear thickening in model suspensions of sterically stabilized particles. *J. Rheol.* **40** (4), 531–548.

GADALA-MARIA, F. & ACRIVOS, A. 1980 Shear-induced structure in a concentrated suspension of solid spheres. *J. Rheol.* **24** (6), 799–814.

GADALA-MARIA, F.A. 1979 *The Rheology of Concentrated Suspensions*. Stanford University.

GALLIER, S., LEMAIRE, E., PETERS, F. & LOBRY, L. 2014 Rheology of sheared suspensions of rough frictional particles. *J. Fluid Mech.* **757**, 514–549.

GALLIER, S., PETERS, F. & LOBRY, L. 2018 Simulations of sheared dense noncolloidal suspensions: evaluation of the role of long-range hydrodynamics. *Phys. Rev. Fluids* **3** (4), 042301.

GILBERT, D. 2021 Rôle des contacts adhésifs et frottants dans la rhéologie des suspensions non-Browniennes. PhD thesis, Université Côte d'Azur.

GILBERT, D., VALETTE, R. & LEMAIRE, E. 2022 Impact of particle stiffness on shear-thinning of non-Brownian suspensions. *J. Rheol.* **66** (1), 161–176.

GUY, B.M., HERMES, M. & POON, W.C.K. 2015 Towards a unified description of the rheology of hard-particle suspensions. *Phys. Rev. Lett.* **115** (8), 088304.

GUY, B.M., RICHARDS, J.A., HODGSON, D.J.M., BLANCO, E. & POON, W.C.K. 2018 Constraint-based approach to granular dispersion rheology. *Phys. Rev. Lett.* **121** (12), 128001.

HSU, C.-P., RAMAKRISHNA, S.N., ZANINI, M., SPENCER, N.D. & ISA, L. 2018 Roughness-dependent tribology effects on discontinuous shear thickening. *Proc. Natl Acad. Sci. USA* **115** (20), 5117–5122.

JOHNSON, K.L., KENDALL, K. & ROBERTS, A.D. 1971 Surface energy and the contact of elastic solids. *Proc. R. Soc. Lond.* A **324** (1558), 301–313.

KALLUS, Y. 2016 The random packing density of nearly spherical particles. *Soft Matt.* **12** (18), 4123–4128.

KEENTOK, M. & XUE, S.-C. 1999 Edge fracture in cone-plate and parallel plate flows. *Rheol. Acta* **38** (4), 321–348.

KRIEGER, I.M. 1972 Rheology of monodisperse latices. *Adv. Colloid Interface Sci.* **3** (2), 111–136.

LARSEN, R.J., KIM, J.-W., ZUKOSKI, C.F. & WEITZ, D.A. 2010 Elasticity of dilatant particle suspensions during flow. *Phys. Rev.* E **81** (1), 011502.

LE, A.V.N., IZZET, A., OVARLEZ, G. & COLIN, A. 2023 Solvents govern rheology and jamming of polymeric bead suspensions. *J. Colloid Interface Sci.* **629**, 438–450.

LOBRY, L., LEMAIRE, E., BLANC, F., GALLIER, S. & PETERS, F. 2019 Shear thinning in non-Brownian suspensions explained by variable friction between particles. *J. Fluid Mech.* **860**, 682–710.

LOOTENS, D., VAN DAMME, H., HÉMAR, Y. & HÉBRAUD, P. 2005 Dilatant flow of concentrated suspensions of rough particles. *Phys. Rev. Lett.* **95** (26), 268302.

MADRAKI, Y., HORMOZI, S., OVARLEZ, G., GUAZZELLI, E. & POULIQUEN, O. 2017 Enhancing shear thickening. *Phys. Rev. Fluids* **2** (3), 033301.

MADRAKI, Y., OAKLEY, A., NGUYEN LE, A., COLIN, A., OVARLEZ, G. & HORMOZI, S. 2020 Shear thickening in dense non-Brownian suspensions: viscous to inertial transition. *J. Rheol.* **64** (2), 227–238.

MADRAKI, Y., OVARLEZ, G. & HORMOZI, S. 2018 Transition from continuous to discontinuous shear thickening: an excluded-volume effect. *Phys. Rev. Lett.* **121** (10), 108001.

MARANZANO, B.J. & WAGNER, N.J. 2001*a* The effects of interparticle interactions and particle size on reversible shear thickening: hard-sphere colloidal dispersions. *J. Rheol.* **45** (5), 1205–1222.

MARANZANO, B.J. & WAGNER, N.J. 2001*b* The effects of particle size on reversible shear thickening of concentrated colloidal dispersions. *J. Chem. Phys.* **114** (23), 10514–10527.

MARI, R., SETO, R., MORRIS, J.F. & DENN, M.M. 2014 Shear thickening, frictionless and frictional rheologies in non-Brownian suspensions. *J. Rheol.* **58** (6), 1693–1724.

MARON, S.H. & PIERCE, P.E. 1956 Application of ree-eyring generalized flow theory to suspensions of spherical particles. *J. Colloid Sci.* **11** (1), 80–95.

MERHI, D., LEMAIRE, E., BOSSIS, G. & MOUKALLED, F. 2005 Particle migration in a concentrated suspension flowing between rotating parallel plates: investigation of diffusion flux coefficients. *J. Rheol.* **49** (6), 1429–1448.

MUELLER, S., LLEWELLIN, E.W. & MADER, H.M. 2010 The rheology of suspensions of solid particles. *Proc. R. Soc. Lond.* A **466** (2116), 1201–1228.

NESS, C. & SUN, J. 2016 Two-scale evolution during shear reversal in dense suspensions. *Phys. Rev.* E **93** (1), 012604.

OVARLEZ, G., BERTRAND, F. & RODTS, S. 2006 Local determination of the constitutive law of a dense suspension of noncolloidal particles through magnetic resonance imaging. *J. Rheol.* **50** (3), 259–292.

OVARLEZ, G., MAHAUT, F., DEBOEUF, S., LENOIR, N., HORMOZI, S. & CHATEAU, X. 2015 Flows of suspensions of particles in yield stress fluids. *J. Rheol.* **59** (6), 1449–1486.

PANTINA, J.P. & FURST, E.M. 2005 Elasticity and critical bending moment of model colloidal aggregates. *Phys. Rev. Lett.* **94** (13), 138301.

PETERS, F., GHIGLIOTTI, G., GALLIER, S., BLANC, F., LEMAIRE, E. & LOBRY, L. 2016 Rheology of non-Brownian suspensions of rough frictional particles under shear reversal: a numerical study. *J. Rheol.* **60** (4), 715–732.
PHILLIPS, R.J., ARMSTRONG, R.C., BROWN, R.A., GRAHAM, A.L. & ABBOTT, J.R. 1992 A constitutive equation for concentrated suspensions that accounts for shear-induced particle migration. *Phys. Fluids* A*: Fluid* **4** (1), 30–40.
PINE, D.J., GOLLUB, J.P., BRADY, J.F. & LESHANSKY, A.M. 2005 Chaos and threshold for irreversibility in sheared suspensions. *Nature* **438** (7070), 997–1000.
RASHEDI, A., OVARLEZ, G. & HORMOZI, S. 2020 Engineered transparent emulsion to optically study particulate flows in yield stress fluids. *Exp. Fluids* **61** (2), 1–13.
RICHARDS, J.A., GUY, B.M., BLANCO, E., HERMES, M., POY, G. & POON, W.C.K. 2020 The role of friction in the yielding of adhesive non-Brownian suspensions. *J. Rheol.* **64** (2), 405–412.
SAINT-MICHEL, B., MANNEVILLE, S., MEEKER, S., OVARLEZ, G. & BODIGUEL, H. 2019 X-ray radiography of viscous resuspension. *Phys. Fluids* **31** (10), 103301.
SARABIAN, M., FIROUZNIA, M., METZGER, B. & HORMOZI, S. 2019 Fully developed and transient concentration profiles of particulate suspensions sheared in a cylindrical couette. *J. Fluid Mech.* **862**, 659–671.
SCHATZMANN, M., FISCHER, P. & BEZZOLA, G.R. 2003 Rheological behavior of fine and large particle suspensions. *J. Hydraul. Engng ASCE* **129** (10), 796–803.
SETO, R., MARI, R., MORRIS, J.F. & DENN, M.M. 2013 Discontinuous shear thickening of frictional hard-sphere suspensions. *Phys. Rev. Lett.* **111** (21), 218301.
SINGH, A., MARI, R., DENN, M.M. & MORRIS, J.F. 2018 A constitutive model for simple shear of dense frictional suspensions. *J. Rheol.* **62** (2), 457–468.
SINGH, A., NESS, C., SETO, R., DE PABLO, J.J. & JAEGER, H.M. 2020 Shear thickening and jamming of dense suspensions: the "roll" of friction. *Phys. Rev. Lett.* **124** (24), 248005.
SNOOK, B., BUTLER, J.E. & GUAZZELLI, É. 2016 Dynamics of shear-induced migration of spherical particles in oscillatory pipe flow. *J. Fluid Mech.* **786**, 128.
SOSIO, R. & CROSTA, G.B. 2009 Rheology of concentrated granular suspensions and possible implications for debris flow modeling. *Water Resour. Res.* **45** (3), W03412.
TRIPATHI, A., KUMAR, V., AGARWAL, A., TRIPATHI, A., BASU, S., CHAKRABARTY, A. & NAG, S. 2021 Quantitative DEM simulation of pellet and sinter particles using rolling friction estimated from image analysis. *Powder Technol.* **380**, 288–302.
VANCE, K., SANT, G. & NEITHALATH, N. 2015 The rheology of cementitious suspensions: a closer look at experimental parameters and property determination using common rheological models. *Cement Concrete Comp.* **59**, 38–48.
VÁZQUEZ-QUESADA, A., MAHMUD, A., DAI, S., ELLERO, M. & TANNER, R.I. 2017 Investigating the causes of shear-thinning in non-colloidal suspensions: experiments and simulations. *J. Non-Newtonian Fluid Mech.* **248**, 1–7.
VÁZQUEZ-QUESADA, A., TANNER, R.I. & ELLERO, M. 2016 Shear thinning of noncolloidal suspensions. *Phys. Rev. Lett.* **117** (10), 108001.
VINCENT, L. & SOILLE, P. 1991 Watersheds in digital spaces: an efficient algorithm based on immersion simulations. *IEEE Comput. Archit. L.* **13** (06), 583–598.
WENSRICH, C.M. & KATTERFELD, A. 2012 Rolling friction as a technique for modelling particle shape in DEM. *Powder Technol.* **217**, 409–417.
WENSRICH, C.M., KATTERFELD, A. & SUGO, D. 2014 Characterisation of the effects of particle shape using a normalised contact eccentricity. *Granul. Matt.* **16** (3), 327–337.
VAN DER WERFF, J.C. & DE KRUIF, C.G. 1989 Hard-sphere colloidal dispersions: the scaling of rheological properties with particle size, volume fraction, and shear rate. *J. Rheol.* **33** (3), 421–454.
WILDEMUTH, C.R. & WILLIAMS, M.C. 1984 Viscosity of suspensions modeled with a shear-dependent maximum packing fraction. *Rheol. Acta* **23** (6), 627–635.
WYART, M. & CATES, M.E. 2014 Discontinuous shear thickening without inertia in dense non-Brownian suspensions. *Phys. Rev. Lett.* **112** (9), 098302.
YOSHIMURA, A. & PRUD'HOMME, R.K. 1988 Wall slip corrections for couette and parallel disk viscometers. *J. Rheol.* **32** (1), 53–67.
ZARRAGA, I.E., HILL, D.A. & LEIGHTON, D.T. JR. 2000 The characterization of the total stress of concentrated suspensions of noncolloidal spheres in Newtonian fluids. *J. Rheol.* **44** (2), 185–220.
ZHOU, J.Z.Q., UHLHERR, P.H.T. & LUO, F.T. 1995 Yield stress and maximum packing fraction of concentrated suspensions. *Rheol. Acta* **34** (6), 544–561.